


Spectroscopic evidence of nematic fluctuations in LiFeAs

Zhixiang Sun,¹ Pranab Kumar Nag,¹ Steffen Sykora,¹ Jose M. Guevara,¹ Sven Hoffmann,¹ Christian Salazar,¹ Torben Hänke,¹ Rhea Kappenberger,^{1,2} Sabine Wurmehl,^{1,2} Bernd Büchner,^{1,2,3} and Christian Hess^{1,3,*}

¹*IFW Dresden, 01069 Dresden, Germany*

²*Institute for Solid State Physics, TU Dresden, 01069 Dresden, Germany*

³*Center for Transport and Devices, TU Dresden, 01069 Dresden, Germany*

 (Received 8 November 2018; revised manuscript received 8 April 2019; published 11 July 2019)

The role of nematic fluctuations in the pairing mechanism of iron-based superconductors is frequently debated. Here, we present a method to reveal such fluctuations by identifying the energy and momentum of the corresponding nematic boson through the detection of a boson-assisted resonant amplification of Friedel oscillations. Using Fourier-transform scanning tunneling spectroscopy, we observe for the unconventional superconductor LiFeAs strong signatures of bosonic states at momentum $q \sim 0$ and energy $\Omega \approx 8$ meV. We show that these bosonic states survive in the normal conducting state, and, moreover, that they are in perfect agreement with well-known strong above-gap anomalies in the tunneling spectra. Attributing these small- q boson modes to nematic fluctuations, we provide a spectroscopic approach to the nematic boson in an unconventional superconductor.

DOI: [10.1103/PhysRevB.100.024506](https://doi.org/10.1103/PhysRevB.100.024506)

I. INTRODUCTION

The identification of the fine structure of tunneling spectra of strong-coupling conventional superconductors with the fingerprints of the phononic Cooper pairing glue counts as a fundamental step in the rationalization of superconductivity [1,2]. The extension of this approach to unconventional superconductors, such as cuprates and iron-based superconductors (IBSs), is highly desirable for clarifying the nature of superconductivity in these materials. However, despite the salient above-gap anomalies often present in tunneling spectra [3–8], their interpretation typically remains elusive. A major reason, apart from difficulties in differentiating between elastic and inelastic tunneling contributions [9], is the lack of momentum information. An accurate resolution of spectral properties in momentum space is, however, crucial for rationalizing superconductivity in multiband materials such as IBSs.

In many canonical IBSs superconductivity emerges upon doping from an antiferromagnetic spin-density-wave (SDW) parent state which probably is related to Fermi-surface nesting [10]. The SDW state furthermore seems intimately connected with unidirectional electronic, so-called nematic order, involving orbital degrees of freedom [11]. These proximities of superconductivity and antiferromagnetic order on the one hand and nematic order on the other have nourished pertinent scenarios for the mechanism of the Cooper pairing, i.e., respectively, antiferromagnetic spin fluctuations [12] and orbital fluctuations [13] are conjectured to drive the superconductivity in the IBS.

A strong antiferromagnetic spin resonance, which would be supportive of the spin fluctuation scenario, has been detected in inelastic neutron scattering for some of the

prototypical IBSs [14]. While similar spectroscopic signatures of nematic fluctuations supporting superconductivity, however, do not exist up to present, evidence for the relevance of small- q nematic fluctuations for superconductivity has been accumulating [11]. Prominent recent examples are *static* small- q electronic density variations observed in tunneling experiments on FeSe thin films [15] and strained LiFeAs [16], where superconductivity is suppressed. Theoretically, the influence of *dynamic* nematic fluctuations can be modeled by a coupling of itinerant electrons to Ising nematic bosons within the framework of an Eliashberg treatment [17]. These small-momentum nematic modes play a role similar to that of phonons in a conventional superconductor with the difference that the pairing potential becomes strongly momentum dependent, is attractive in all pairing channels, and so enhances T_c [17]. A generalization of this model to a system of coupled fermion bond density and pseudospin-1/2 degree of freedom has been solved by quantum Monte Carlo simulations [18] and the enhancement of superconducting pairing has been confirmed.

Here, we report spectroscopic evidence of such small-momentum bosonic modes representing nematic fluctuations. To this end, we exploit a combined theoretical and experimental approach for detecting the signatures of bosonic degrees of freedom in quantum materials using Fourier-transform scanning tunneling spectroscopy (FT-STs) experiments. FT-STs is well established to detect the momentum space representation of the so-called quasiparticle interference (QPI), i.e., the Fourier transform of real-space wavelike modifications of the local density of states (LDOS) caused by an impurity, i.e., the Friedel oscillations. The *geometry* of the Friedel oscillations in momentum space has successfully been used to reconstruct the electronic band structure of many correlated materials [20–27]. This includes, since very recently, even the detection of subtle band renormalizations due to

*c.hess@ifw-dresden.de

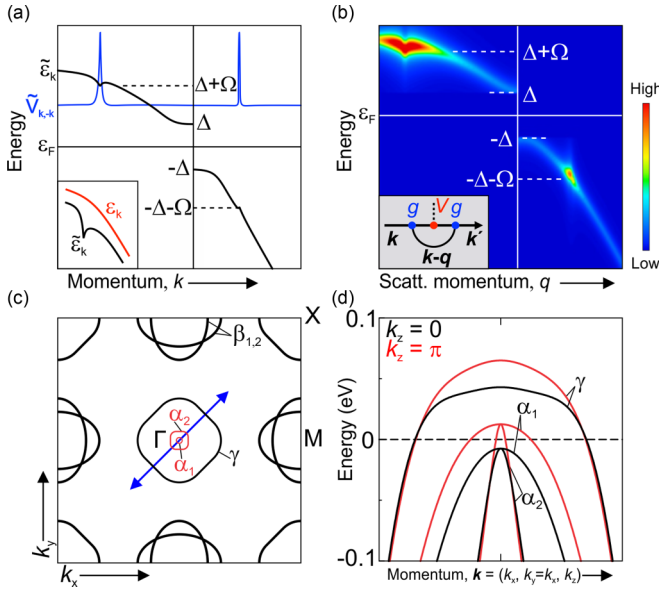


FIG. 1. Illustration of the boson-enhanced QPI and of the fermiology of LiFeAs. (a) Sketch of a holelike band $\tilde{\epsilon}_k$ (black) in the superconducting state which is renormalized due to electron-boson coupling giving rise to the well-known kinklike structures above and below the Fermi level at energies indicated by dashed lines (the inset shows the bare band in red). Blue line: Renormalized impurity potential $\tilde{V}_{k,-k}$ combining opposite momentum vectors representing relevant elastic scattering processes in the QPI. The renormalization is strong at the particular \mathbf{k} points of the kink structure. (b) Sketch of the Fourier-transformed LDOS arising from the renormalized quantities $\tilde{\epsilon}_k$ and $\tilde{V}_{k,-k}$ of (a) (see Appendix A 1). The intensity is strongly enhanced around the particular scattering momentum combining points where both the fermion band as well as the impurity scattering potential are strongly renormalized due to electron-boson coupling. Inset: Feynman diagram of the corresponding dominant scattering process which is dressed by the excitation of a virtual bosonic mode. (c) Illustration of the FS of LiFeAs [19]. Black: Projection of quasi-two-dimensional FS pockets to the $k_z = 0$ plane. Red: FS pockets of the α bands at $k_z = \pi$ (Z point) which appear only near this point. (d) Dispersion of the holelike bands along the blue arrow in (c) for $k_z = 0$ (black) and $k_z = \pi$ (red).

electron-boson interactions [25–27]. Despite this enormous success of QPI analysis, the impact of the electron-boson interaction on the Friedel oscillation itself has remained largely unexplored. We have investigated this aspect theoretically (see Appendix A 1 for details) and find that the impurity scattering potential and thus the *amplitude* of the QPI is resonantly enhanced if the involved electronic states are interacting with a boson [see Figs. 1(a) and 1(b)]. The effect is strong and implies that an amplitude analysis of the QPI can yield signatures of an interacting boson, including specific information about the bosonic momentum and energy. The exploitation of this effect in tunneling experiments can therefore be viewed as the addition of momentum information to the analysis of bosonic signatures in tunneling spectroscopy. We particularly point out that our method can be used to detect a boson independently of its nature, i.e., the boson could be the effective representation of spin, charge, orbital, or nematic fluctuations, or it describes phonons. The mentioned amplitude sensitivity is here

exploited to investigate the unconventional superconductor LiFeAs, where the method works particularly well, as we will show below.

LiFeAs differs in its properties from most other IBSSs for the following reasons: It is a stoichiometric superconductor which shows no sign of Fermi-surface nesting [28,29] and no magnetic or nematic order, even under doping [30,31]. Instead of an antiferromagnetic spin resonance, only weak signatures of spin excitations are observed at incommensurate positions in momentum space [32] which are understood to arise from interband transitions between the quasi-two-dimensional large holelike and the electronlike Fermi-surface (FS) pockets [labeled γ and β , respectively—see Fig. 1(c)] [33]. In fact, these weak spin fluctuations exhibit only subtle changes upon switching between the normal and superconducting state which renders these fluctuations poor candidates for providing the superconducting pairing interaction.

In spite of all this, LiFeAs has a relatively large critical temperature T_c of about 18 K [31], supporting the idea that an alternative intrinsic mechanism which enhances the superconducting pairing could be relevant in LiFeAs. This material thus is, among the IBSSs, an ideal candidate to search for evidence of small-momentum nematic mode bosons which couple to the electronic states and stabilize the pairing. Indeed, small-momentum electronic states in connection to the small three-dimensional FS droplets arising from holelike bands (labeled α) along the Γ - Z direction have been assigned an important role for the superconducting state [19,34] [Fig. 1(d)]. Interestingly, the superconducting gap has been observed to be significantly larger for these α states ($\Delta_1 \approx 6$ meV) as compared to that of the β and γ bands ($\Delta_2 \lesssim 4$ meV) [35], which indeed suggests that the strongest pairing interaction in LiFeAs primarily involves states of these bands [cf. Fig. 2(a) for the signatures of Δ_1 and Δ_2 in low-temperature tunneling spectra].

Previous FT-STs studies of LiFeAs [22–24,26,36] have not specifically addressed these α bands in the required energy and temperature range to reveal their connection to superconductivity. A possible reason is that these states are located at very small in-plane momenta which requires a particularly high resolution in momentum space. In order to achieve this high resolution in our QPI experiments, we recorded large ($110 \text{ nm} \times 110 \text{ nm}$) spectroscopic maps of LiFeAs, where we measured the differential conductance $dI/dU(U_{\text{bias}})$ as a direct access to the LDOS (see Appendix B for experimental details). The measurements of these maps have furthermore been performed at several temperatures ranging from 6.7 K up to 25 K to cover the QPI evolution from the superconducting state to the normal conducting state and to explore a possible temperature evolution of bosonic mode signatures.

II. RESULTS

Here, we show our experimental results of spectroscopic tunneling measurements of LiFeAs in the superconducting and normal conducting state. From these data we reveal a resonance in the QPI which we assign to a boson representing the nematic fluctuations in LiFeAs.

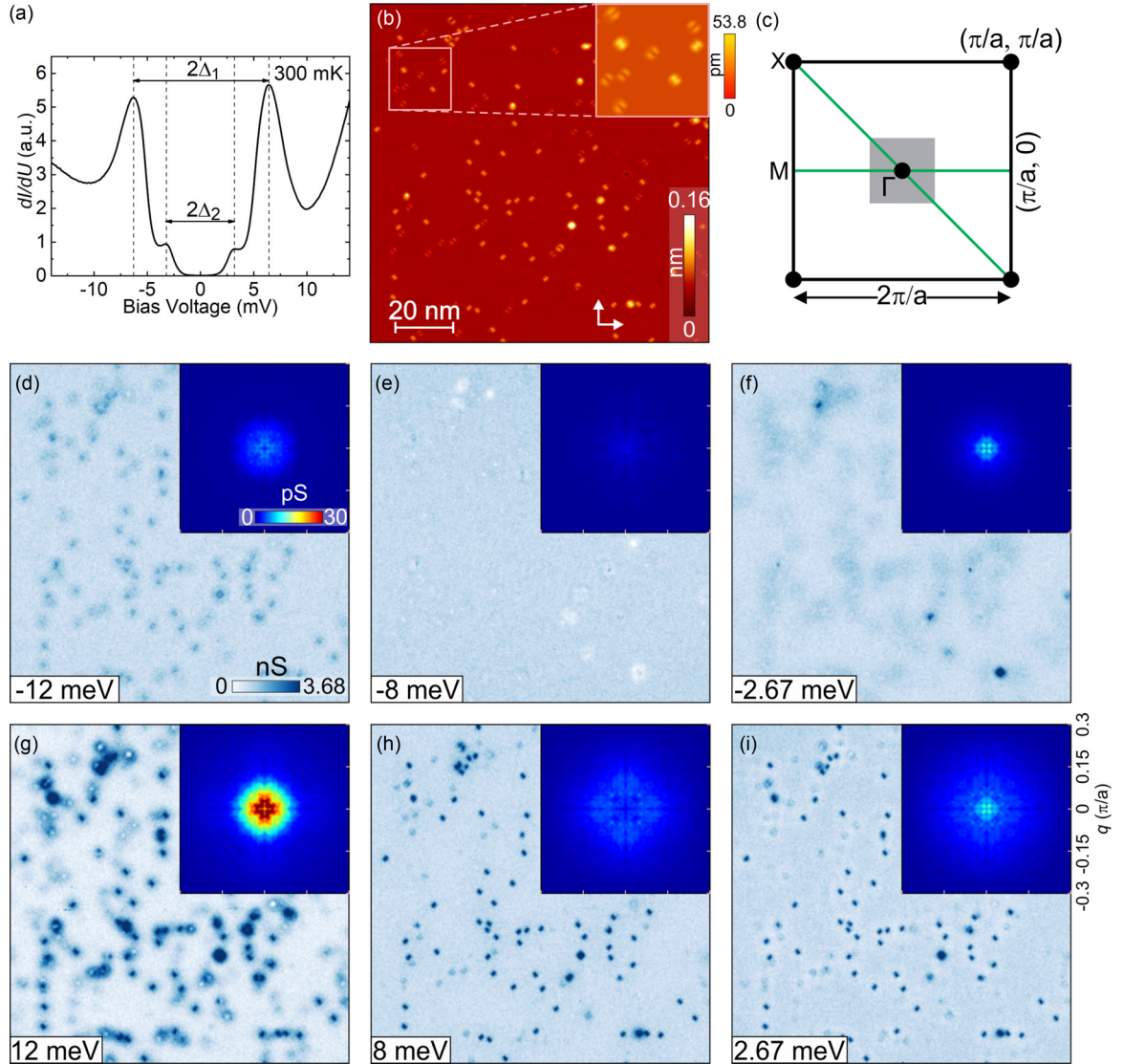


FIG. 2. Experimental spectroscopic tunneling data in the superconducting state. (a) Average dI/dU spectrum measured on a defect-free surface area of LiFeAs at $T = 300$ mK. (b) A representative surface topography ($U_{\text{bias}} = -50$ mV, $I = 100$ pA) with clearly identifiable Fe defects (inset). The directions of the shortest Fe-Fe distance $a = 2.68$ Å [31] are indicated by arrows. (c) Illustration of the space of in-plane scattering vectors. Green lines indicate the high-symmetry directions considered in Fig. 3. The gray square shows the q -space area covered by the insets in (d)–(i). (d)–(i) Real-space conductance map data recorded at $T = 6.7$ K at energies $eU_{\text{bias}} = \pm 12, \pm 8, \text{ and } \pm 2.67$ meV. All conductance map data are taken in the same area as shown in (b). The Fourier transformation of the real-space conductance map data is shown in the corresponding insets.

A. Quasiparticle interference

Figure 2(b) depicts representative topographic data of a cleaved surface where the spectroscopic maps have been recorded. In these data one can recognize primarily the typical dumbbell-like iron site defects/impurities (135 defects in total, corresponding to a defect concentration of less than 0.1% with respect to Fe), which have frequently been observed in LiFeAs [22,23,37,38]. They serve as the main scattering centers in the sample. In Figs. 2(d)–2(i), we present the spectroscopic map data in the superconducting state at 6.7 K for several selected energy values (see Appendix C and the Supplemental Material [39] for a comprehensive representation of the whole data set). From these data not only is the profound impact of the impurities on the LDOS in their

vicinity of several nanometers apparent. It is also very evident that this impact is strongly energy dependent: The relative conductance change around the impurities remains relatively subtle at $E \leq 8$ meV. However, at $E = 12$ meV, the dI/dU variation around the impurities becomes very strong, and acquires a much larger extension. This is also recognizable in the Fourier-transformed data (see Appendix B for a description of the method) shown in the insets of Figs. 2(d)–2(i) (see also Appendix C). For $E \leq 8$ meV, the QPI signal always remains below about 10 pS but significantly exceeds this value at $E = 12$ meV.

In order to highlight the pronounced energy and momentum dependence of the Fourier-transformed data, we plot in Figs. 3(a) and 3(b) line cuts of the QPI pattern along the

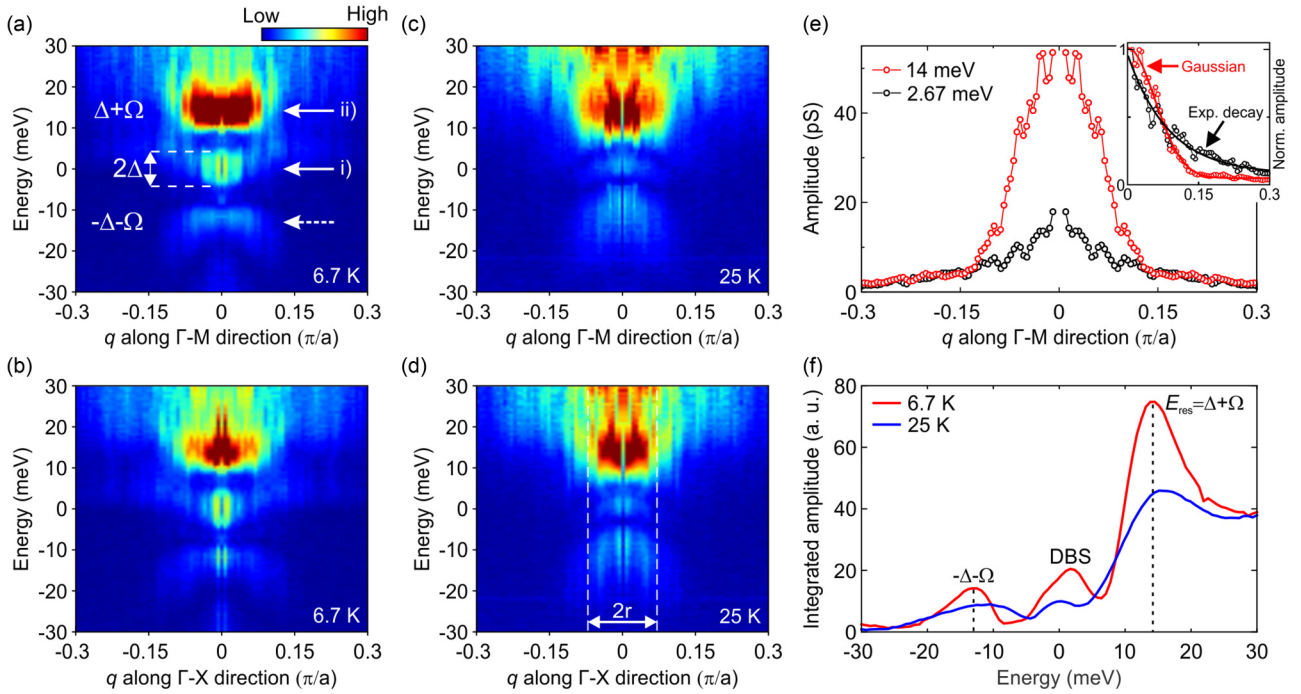


FIG. 3. Energy and momentum dependence of the FT-STs data in the superconducting and the normal conducting state. (a)–(d) QPI line cuts along the high-symmetry directions [cf. Fig. 2(c)] for the conductance maps taken in the superconducting phase at $T = 6.7$ K [(a) and (b)] and in the normal phase at $T = 25$ K [(c) and (d)]. Solid line arrows in (a) indicate the energetic position of features (i) and (ii), whereas the dashed line arrow indicates the “replica” of feature (ii) at negative energy. (e) QPI intensity as a function of q along Γ -M of feature (ii) and feature (i) at 14 and 2.67 meV, respectively. Inset: The same data normalized at $q \sim 0$. The solid lines represent fits according to an exponential decay $\propto \exp(-\alpha q)$ and a Gaussian for feature (i) and feature (ii), respectively. (f) Integrated QPI density at $|q| < r = 0.07\pi/a$ [as indicated in (d)] for the 6.7- and 25-K data. Signatures of the enhanced QPI signal are visible at both positive and negative energy, where a pronounced enhancement occurs in the superconducting state. The FT-STs signature [feature (i)] caused by defect bound states (DBSs) is visible as well.

two high-symmetric directions as illustrated by the green lines in Fig. 2(c). This data representation reveals a relatively weak anisotropy and two main features [labeled (i) and (ii) in Fig. 3(a)] at small momenta $q \lesssim 0.1\frac{\pi}{a}$ which correspond to large wavelength modulations in real space.

Feature (i) occurs at $|E| \lesssim 6$ meV, i.e., its energy range coincides with the large superconducting gap Δ_1 . This strong in-gap intensity is incompatible with conventional QPI arising from quasiparticle intra- or interband scattering processes, obviously because of the absence of quasiparticle states in this energy range. Instead, this structure can straightforwardly be attributed to defect/impurity bound states of LiFeAs. The QPI intensity that arises from these particular states is expected to occur strictly within the superconducting gap energy range. Furthermore, feature (i) decays rapidly with increasing q and thus reproduces other studies which show clearly that the intensity of the bound states emanate outward from the center of an impurity on a length scale of a few nanometers [37,38,40]. The connection of feature (i) to impurity bound states and thus to the superconducting state can be further corroborated by an investigation of its temperature dependence across the critical temperature. Here, we observe the feature to fade out, as expected [see Figs. 3(c) and 3(d) for $T = 25$ K, as well as Appendix C for intermediate-temperature data]. At the highest temperature studied ($T = 25$ K) there remains just a weak intensity around $E = 0$ which accounts for the impact of the impurity on the LDOS in the normal conducting state.

After having established the rather conventional nature of the in-gap intensity, we turn now to analyzing feature (ii) which by far dominates the data. This structure has a sharp onset at about 10 meV and extends up to about 22 meV with a maximum at $E_{\text{res}} \approx 14$ meV. It is sharply peaked at $q \sim 0$, and has a much larger amplitude than feature (i) [see Fig. 3(e)]. Moreover, while the latter decays exponentially in q , the momentum dependence of feature (ii) is well described by a Gaussian [inset of Fig. 3(e)]. This functional variation is remarkable and excludes long-wavelength spatial noise as the origin of our observations. At first glance, the occurrence of such a strong intensity in this energy range significantly away from the superconducting gap appears surprising. Clearly, it cannot be the direct signature of an impurity bound state because such a state would exist strictly only within the superconducting gap energy [41]. Furthermore, conventional QPI arising from intra- or interband scattering processes within the two α bands (which in principle would be compatible with the relatively small q value) at first glance cannot account for this observation: It is well known that the α bands possess a strong k_z dispersion [19,42]. Thus, the QPI signal that emerges from these bands normally should be very broad and featureless in energy and momentum. This is because the QPI that is measured by scanning tunneling spectroscopy (STS) is *a priori* not sensitive to the k_z . At a given energy, the measured QPI pattern is expected to be a result of the superposition of all different in-plane (i.e., $\Delta k_z = 0$) scattering wave vectors at

different k_z and the in-plane projection of scattering vectors with finite Δk_z . Since the scattering vectors must combine points of equal energy, a k_z dispersion is always related to a certain broadening in the (k_x, k_y) direction. Indeed, one might conjecture that the faint and broad QPI structures of rather low amplitude lower than ~ 5 pS as seen for example in Fig. 2(h) are compatible with this picture. In contrast, the observed extraordinary enhancement of intensity in the particular energy range of feature (ii) cannot be explained in this way and therefore directly implies an unusual amplification of the measured QPI. In fact, feature (ii) can straightforwardly be interpreted as resonantly enhanced QPI due to a boson-assisted renormalization of scattering potential as is illustrated in Figs. 1(a) and 1(b). More specifically, this scenario implies feature (ii) to be caused by bosons centered at energy Ω and momentum $q \sim 0$, where $E_{\text{res}} = \Delta + \Omega$, with Δ the superconducting gap (Appendix A 1).

Before we discuss the possible implications of the detection of pertinent bosonic excitations with small momentum, we investigate further corroborations of this fundamental finding. First, the electron-boson interaction must concern not only the unoccupied states (as discussed so far) but also the occupied electronic states. Indeed, the close inspection of the data shown in Figs. 3(a) and 3(b), reveals, despite an overall weaker amplitude, a pronounced enhancement of the QPI signal at about $-E_{\text{res}} = -\Delta - \Omega$ (dashed arrow). Second, feature (ii) is significantly more intense than robust QPI signatures at larger wave vectors. This can be inferred from the additional data set in Appendix D, where we explicitly compare the integrated intensity of feature (ii) with well-known nested intraband scattering within the γ band.

Interestingly, the signature of the boson persists in the whole temperature regime up to the normal conducting state far above the critical temperature at $T = 25$ K, as is revealed by the inspection of our temperature dependent QPI data [see Figs. 3(c), 3(d), and also Fig. 12 in Appendix C 3]. The difference between the superconducting and normal conducting states is further illustrated in Fig. 3(f), where we show the integrated QPI intensity over the region with $|q| < r = 0.07 \frac{\pi}{a}$ [cf. Fig. 3(d)] as a function of the energy for both $T = 6.7$ K and $T = 25$ K. The data for the superconducting state show clearly that there are resonancelike peaks with a quite sharp onset at around ± 10 meV with peak values at about $\pm(13 \dots 14)$ meV, where the peak at positive energy is much more pronounced. Both peaks broaden in the normal conducting state where the low-energy edge shifts to about ± 5 meV, whereas the peak positions, in particular, that of the better resolved peak at positive energy, barely change. Qualitatively, the sharpening of the peaks in the superconducting state can be rationalized as a direct consequence of the formation of Bogoliubov quasiparticle states and a further, resonancelike enhancement of the QPI signal at $E_{\text{res}} = \Delta + \Omega$ by an exaggeration of the scattering potential due to coupling to the bosons. We extract, by focusing on the better resolved peak in the superconducting state at positive energy where $E_{\text{res}} = 14 \pm 4$ meV and by employing the gap at the α states $\Delta_1 = 6$ meV [35], a mode peak energy $\Omega = 8 \pm 4$ meV [43].

At first glance it seems surprising that the resonance peak remains practically unshifted in energy upon entering the normal state. In order to obtain further insight into the nature

of our observation we performed a careful theoretical analysis of the impurity scattering in LiFeAs using realistic parameters for band structure (including the spin-orbit coupling [42]), scattering potential, and electron-boson coupling (see Appendix A 2). A central finding of this analysis is that, due to the particular structure of the α bands in LiFeAs, which encompasses a spin-orbit coupling induced separation of the band maxima with a high density of states by approximately the same amount (of the order of 10 meV) than Δ_1 , the resonance conditions in the normal state are accidentally similar to that of the superconducting state. Indeed, the analysis yields a consistent description of the observed resonance in both phases, explaining the absence of a shift of the peaks. A further important and interesting result of this analysis is that the interaction of the considered boson with the band structure of LiFeAs leads to a stable superconducting solution with the leading experimental gap value at the α states.

It further is interesting to verify our finding of a small-momentum boson against optical spectroscopy where signatures of electron-boson coupling at $q \sim 0$ should be well detectable. Indeed, a recent optical study [44] which reveals a $q = 0$ mode at the very same energy underpins our finding, however, lacking the general momentum sensitivity and resolution which is provided by the analysis of resonantly enhanced QPI as presented in this work.

B. Comparison with tunneling spectroscopy

Another, alternative way to identify the signature of bosonic excitations is the investigation of tunneling dI/dU spectra far away from impurities, where bosonic excitations may leave their fingerprints in two fundamentally different ways: On the one hand, bosonic excitations which couple to Bogoliubov quasiparticles of a superconductor may induce a characteristic fingerprint in the tunneling spectra if the coupling is strong enough. More specifically, a well-defined bosonic mode at energy Ω is expected to give rise to a peak structure at the energy $\Delta + \Omega$ (with Δ the superconducting gap) [1,2] [see Fig. 4(a)]. On the other hand, bosonic excitations may open up a relevant *inelastic* scattering channel in addition to the usual elastic one, playing a dominant role in the dI/dU in unconventional superconductors, and particularly in LiFeAs [9]. In the case of a relevant inelastic tunneling contribution due to a well-defined boson, a significant enhancement of the tunneling dI/dU is expected for $E > \Delta + \Omega$ and $E > \Omega$ in the superconducting and the normal conducting states, respectively [Fig. 4(b)]. As is shown in Figs. 4(b) and 4(c), this leads to a characteristic depletion and steplike enhancement of the dI/dU in the superconducting state with respect to that of the normal conducting state at $E < \Delta + \Omega$ and $E > \Delta + \Omega$, respectively.

We therefore show in Fig. 4(d) a direct comparison of the dI/dU for both the superconducting state and the normal conducting state and investigate the data for fingerprints of the boson that we have identified from the QPI data. Quite clearly, the data show dominant signatures of inelastic tunneling: At energies close to the gap edges, dI/dU of the superconducting state exhibits a depletion with respect to that of the normal state whereas it shows a steplike enhancement at about 14 meV and exceeds the dI/dU of the normal state beyond.

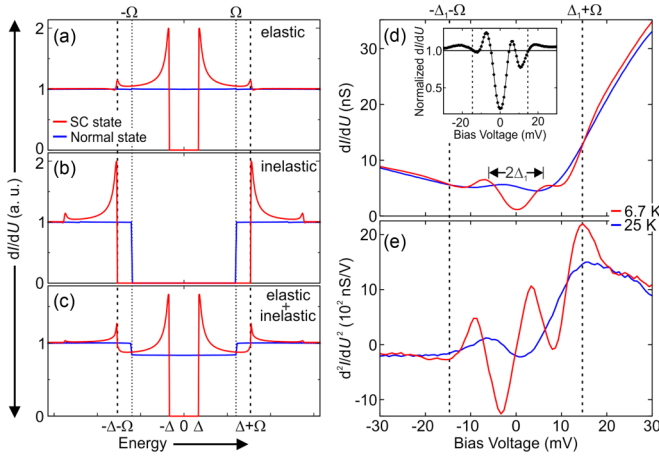


FIG. 4. Impact of bosonic excitations on tunneling spectra. (a)–(c) Calculated (a) elastic and (b) inelastic contributions to the dI/dU spectrum both in the superconducting (SC) and the normal conducting state (red and blue lines, respectively) for the simplified model of electron-boson coupling (boson energy Ω , superconducting gap Δ) as described in Appendix A 1. The theoretical approach to the inelastic contributions is taken from Ref. [9]. For the total tunneling spectrum shown in (c) the ratio of elastic and inelastic contribution is fixed by the chosen model parameters. The combination of the two different contributions leads in an energy range between Ω and $\Delta + \Omega$ to the characteristic depletion of spectral weight in the superconducting state with respect to the normal conducting state. This depletion results in a characteristic dip-hump structure in normalized tunneling spectra [9]. (d) Average dI/dU spectra measured on defect-free surface areas in the superconducting (6.7 K, red) and normal conducting state (25 K, blue). Inset: dI/dU spectrum at 6.7 K normalized with respect to the normal conducting state spectrum at 25 K revealing the dip-hump structure. (e) Voltage derivative d^2I/dU^2 of the data in (d). The dashed lines in both polarities through (a) to (e) indicate the inelastic peak position.

This energy dependence leads to the known characteristic “dip-hump” anomaly in normalized dI/dU data [9], which is often observed in various unconventional superconductors, including LiFeAs [3–8,40] [inset of Fig. 4(d)]. Since the steplike increase of the dI/dU in the superconducting state at about 14 meV [cf. Fig. 4(e)] is expected to occur at $\Delta + \Omega$, we extract $\Omega = 8 \pm 4$ meV if we use $\Delta_1 = 6$ meV as the leading gap [43]. Thus, this completely different approach of accessing the bosonic excitations in LiFeAs yields a boson energy in excellent agreement with our QPI analysis. This suggests that the salient above-gap structure in the local dI/dU tunneling spectra of LiFeAs result from the *same* small-wave-vector bosonic mode which we infer from our QPI data. Scenarios which interpret the nature of the dip-hump structure in terms of an antiferromagnetic spin resonance [7,9,40] can therefore be excluded. It is interesting to point out that the intrinsic width of the step is not significantly reduced in tunneling spectra at very low temperature (see Appendix C for data at 300 mK) despite a significant sharpening of the thermal width of the coherence peaks. This suggests that the energetic width of the involved boson is not sharp, indicative of the importance of many-body effects for the nature of the boson.

III. CONCLUSIONS

Our identification of bosonic modes at $\Omega \approx 8$ meV with a small wave vector q and a connected resonancelike enhancement of the QPI signal in the superconducting state provides fresh input and constraints for rationalizing the pairing mechanism of LiFeAs [19,34,45–47]. The observed incommensurate spin fluctuations definitely can be excluded as a microscopic origin for our observations because inelastic neutron scattering proves a too large wave vector and a negligible difference between the normal and the superconducting states [32]. A further alternative but rather exotic origin of our bosonic mode could be small- q spin fluctuations, which have been derived in model calculations [45], but have not yet experimentally been observed. The final remaining microscopic origin of the mode which is consistent with our analysis lies in *dynamic* nematic or small- q electronic density fluctuations, representing a pertinent instability of the system. In this context it is important to note that static small- q electronic density fluctuations have been observed experimentally in strained LiFeAs [16] and that nematicity induced by the superconductivity has been reported in a recent angle-resolved photoemission spectroscopy (ARPES) study [48].

In this context it is important to emphasize recent scanning tunneling microscopy (STM) results of Ref. [16] on strained LiFeAs, where a static form of the nematic fluctuations, i.e., a rotational symmetry broken phase with long-range small-wave-vector density variations, and a concomitant suppression of superconductivity is observed. The interpretation of small-momentum excitations observed in our study as dynamic nematic fluctuations is therefore strongly corroborated. Furthermore, the reported suppression of superconductivity upon the onset of charge-density-wave order supports our conclusion that the “nematic” small-wave-vector density fluctuations are crucial for sustaining superconductivity in LiFeAs.

ACKNOWLEDGMENTS

We acknowledge fruitful discussions with S. Borisenko, M. Braden, I. Eremin, D. van der Marel, M. Vojta, and P. Wahl. We further thank U. Nitzsche, U. Gräfe, and D. Baumann for technical assistance. This project has been supported by the Deutsche Forschungsgemeinschaft through the Priority Programme SPP 1458 (Grants No. HE 3439/11 and No. BU 887/15-1) and through GRK 1621. S.W. acknowledges funding by the Deutsche Forschungsgemeinschaft under the Emmy-Noether program (Grant No. WU 595/3-3). T.H. acknowledges support by the Deutsche Forschungsgemeinschaft under Grant No. HA 6037/2-1. Furthermore, this project has received funding from the European Research Council (ERC) under the European Unions’ Horizon 2020 research and innovation programme (Grant Agreement No. 647276–MARS–ERC–2014–CoG).

APPENDIX A: THEORY

Here, we present our theoretical approach to the observed resonance feature in the QPI. Starting from a general treatment of impurity scattering in the presence of an

electron-boson interaction, we show that an exaggerated effect is particularly obtained in the specific situation of LiFeAs.

1. Renormalization of the scattering potential

We consider one single local impurity embedded in a system of conduction electrons which additionally couples to a system of bosons. Of particular interest is the change of the electronic local density of states in the environment of the impurity due to elastic scattering of quasiparticles interacting via virtual bosonic excitations. The calculated effect to the local density of states variations is compared with STS measurements in LiFeAs. To avoid taking into account additional effects from the band structure we consider here a single parabolic band and the simplest possible form of electron-boson coupling and impurity scattering. The model Hamiltonian for such a system consists of three parts, $\mathcal{H} = \mathcal{H}_0 + \mathcal{H}_V + \mathcal{H}_{eb}$, where

$$\begin{aligned}\mathcal{H}_0 &= \sum_{\mathbf{k},\sigma} \varepsilon_{\mathbf{k}} c_{\mathbf{k},\sigma}^\dagger c_{\mathbf{k},\sigma} + \sum_{\mathbf{q}} \omega_{\mathbf{q}} b_{\mathbf{q}}^\dagger b_{\mathbf{q}}, \\ \mathcal{H}_{eb} &= \frac{1}{\sqrt{N}} \sum_{\mathbf{k},\mathbf{q},\sigma} g_{\mathbf{k},\mathbf{q}} (b_{\mathbf{q}}^\dagger c_{\mathbf{k},\sigma}^\dagger c_{\mathbf{k}+\mathbf{q},\sigma} + b_{\mathbf{q}} c_{\mathbf{k}+\mathbf{q},\sigma}^\dagger c_{\mathbf{k},\sigma}), \\ \mathcal{H}_V &= \frac{1}{N} \sum_{\mathbf{k},\mathbf{q},\sigma} V_{\mathbf{k},\mathbf{q}} (c_{\mathbf{k},\sigma}^\dagger c_{\mathbf{k}+\mathbf{q},\sigma} + c_{\mathbf{k}+\mathbf{q},\sigma}^\dagger c_{\mathbf{k},\sigma}).\end{aligned}$$

Here, N is the number of lattice sites. The first term describes a system of free conduction electrons and bosons. Thereby, the operator $c_{\mathbf{k},\sigma}^\dagger$ creates an electron with momentum \mathbf{k} (dispersion $\varepsilon_{\mathbf{k}}$) and spin σ and the operator $b_{\mathbf{q}}^\dagger$ creates a boson with momentum \mathbf{q} (dispersion $\omega_{\mathbf{q}}$). The coupling between electrons and bosons is represented by the second term \mathcal{H}_{eb} . It describes the scattering of an electron between states \mathbf{k} and $\mathbf{k} + \mathbf{q}$ while a boson with momentum \mathbf{q} is created or annihilated. The corresponding parameter of the coupling strength $g_{\mathbf{k},\mathbf{q}}$ generally depends on the contributing momentum vectors accounting for a possible nonlocal electron-boson interaction. The term \mathcal{H}_V describes the scattering interaction off the single impurity with the momentum-dependent scattering potential $V_{\mathbf{k},\mathbf{q}}$. Note that this part breaks the translation symmetry of the Hamiltonian.

The variations of the local density of states due to the impurity scattering in an electron-boson coupled system is calculated as follows. At first the Hamiltonian $\mathcal{H} = \mathcal{H}_0 + \mathcal{H}_V + \mathcal{H}_{eb}$ is mapped to a particular effective Hamiltonian $\tilde{\mathcal{H}} = \tilde{\mathcal{H}}_0 + \tilde{\mathcal{H}}_V$ which is constructed in such a way that the electron-boson coupling is fully integrated out by use of a unitary transformation. The new Hamiltonian has the same form as the original one,

$$\begin{aligned}\tilde{\mathcal{H}} &= \sum_{\mathbf{k},\sigma} \tilde{\varepsilon}_{\mathbf{k}} c_{\mathbf{k},\sigma}^\dagger c_{\mathbf{k},\sigma} + \sum_{\mathbf{q}} \tilde{\omega}_{\mathbf{q}} b_{\mathbf{q}}^\dagger b_{\mathbf{q}} \\ &+ \frac{1}{N} \sum_{\mathbf{k},\mathbf{q},\sigma} \tilde{V}_{\mathbf{k},\mathbf{q}} (c_{\mathbf{k},\sigma}^\dagger c_{\mathbf{k}+\mathbf{q},\sigma} + c_{\mathbf{k}+\mathbf{q},\sigma}^\dagger c_{\mathbf{k},\sigma}),\end{aligned}\quad (\text{A1})$$

but with renormalized energy parameters $\tilde{\varepsilon}_{\mathbf{k}}$, $\tilde{\omega}_{\mathbf{q}}$, and $\tilde{V}_{\mathbf{k},\mathbf{q}}$. It is calculated by using the projective renormalization method (PRM) [49] which has already been successfully applied to solve models with electron-boson interactions [50,51]. Note

that the form of Hamiltonian (A1) is strictly only valid in the normal conducting state. For ordered states the inclusion of symmetry breaking order parameter terms is necessary [51]. Here, we focus on the renormalization of the impurity potential in the third term of Eq. (A1) which can be discussed most clearly in the normal conducting state. The influence of the superconducting order is discussed further below.

Within the PRM approach nonlinear difference equations for the renormalized parameters (renormalization equations) are numerically evaluated starting from the given energy parameters of the original Hamiltonian \mathcal{H} . The effective Hamiltonian (A1) is then taken to calculate the local density of states variations using the standard t -matrix method.

The main effect of the electron-boson coupling is the renormalization of the impurity scattering potential. This can be seen from the result of the renormalized impurity potential $\tilde{V}_{\mathbf{k},\mathbf{q}}$ in *lowest-order perturbation theory* with respect to the original coupling parameters $g_{\mathbf{k},\mathbf{q}}$ and $V_{\mathbf{k},\mathbf{q}}$. The perturbation theory can be easily carried out within the PRM by following the ideas of Ref. [49]. Considering for simplicity momentum-independent coupling parameters of the original Hamiltonian, $g_{\mathbf{k},\mathbf{q}} = g$ and $V_{\mathbf{k},\mathbf{q}} = V$, the lowest-order result for the renormalized impurity potential can be written in the form $V_{\mathbf{k},\mathbf{k}'}^{(2)} = (\tilde{V}_{\mathbf{k},\mathbf{k}'}^{(2)} + \tilde{V}_{\mathbf{k}',\mathbf{k}}^{(2)})/2$, where

$$\begin{aligned}\tilde{V}_{\mathbf{k},\mathbf{k}'}^{(2)} &= V + \frac{Vg}{N} \sum_{\mathbf{q}} \left[\frac{2f_{\mathbf{k}'+\mathbf{q}} - 1}{\varepsilon_{\mathbf{k}'+\mathbf{q}} - \varepsilon_{\mathbf{k}'} + \omega_{\mathbf{q}}} \right. \\ &\times \left(\frac{g}{\varepsilon_{\mathbf{k}'+\mathbf{q}} - \varepsilon_{\mathbf{k}'} + \omega_{\mathbf{q}}} - \frac{g}{\varepsilon_{\mathbf{k}+\mathbf{q}} - \varepsilon_{\mathbf{k}} + \omega_{\mathbf{q}}} \right) \\ &+ \frac{2f_{\mathbf{k}+\mathbf{q}} - 1}{\varepsilon_{\mathbf{k}} - \varepsilon_{\mathbf{k}+\mathbf{q}} + \omega_{\mathbf{q}}} \\ &\times \left. \left(\frac{g}{\varepsilon_{\mathbf{k}'} - \varepsilon_{\mathbf{k}'+\mathbf{q}} + \omega_{\mathbf{q}}} - \frac{g}{\varepsilon_{\mathbf{k}} - \varepsilon_{\mathbf{k}+\mathbf{q}} + \omega_{\mathbf{q}}} \right) \right].\end{aligned}\quad (\text{A2})$$

The function $f_{\mathbf{k}} = 1/(1 + e^{\beta(\varepsilon_{\mathbf{k}} - \varepsilon_F)})$ denotes the Fermi distribution with inverse temperature $\beta = 1/(k_B T)$ and Fermi energy ε_F . Terms proportional to the boson distribution function also arise in the second-order perturbation theory but they can be neglected at low temperatures due to very small boson occupation. Expression (A2) diverges below a characteristic temperature for particular values of the momentum vectors \mathbf{k} and \mathbf{k}' . The divergence appears since at certain momentum vectors \mathbf{q} in the summation the energy denominators become zero while at the same time the Fermi factors $(2f_{\mathbf{k}'+\mathbf{q}} - 1)$ and $(2f_{\mathbf{k}+\mathbf{q}} - 1)$ change their sign.

Since this behavior is essential for the observed resonance-like enhancement of the tunneling density of states, we here explain this renormalization process in more detail. Let us simplify the discussion by considering dispersionless bosons, i.e., $\omega_{\mathbf{q}} = \Omega$. Furthermore, we consider the renormalized scattering potential in Eq. (A2) at a particular fixed momentum vector \mathbf{k}' such that $\varepsilon_{\mathbf{k}'} = \varepsilon_F + \Omega$. In this case the denominator in the first line of Eq. (A2) becomes $\varepsilon_{\mathbf{k}'+\mathbf{q}} - \varepsilon_{\mathbf{k}'} + \omega_{\mathbf{q}} = \varepsilon_{\mathbf{k}'+\mathbf{q}} - \varepsilon_F$. Thus, during the summation over \mathbf{q} this

denominator becomes zero for $\varepsilon_{\mathbf{k}+\mathbf{q}} = \varepsilon_F$ but changes its sign which usually leads to a cancellation of diverging terms. Here, however, the situation is different. Due to the presence of the Fermi distribution the numerator in the first line, $2f_{\mathbf{k}+\mathbf{q}} - 1$, changes its sign exactly at the same \mathbf{q} , namely, for $\varepsilon_{\mathbf{k}+\mathbf{q}} = \varepsilon_F$. Since the factor in parentheses in the second line does not change its sign at this particular \mathbf{q} (for $\mathbf{k} \neq \mathbf{k}'$), the sign of the diverging terms is preserved and we here have a real divergency which cannot be canceled out by summation. From a close inspection of all terms in Eq. (A2) with respect to the above considerations one can conclude that the renormalized scattering potential becomes strongly enhanced when the momentum vectors fulfill roughly the ‘‘resonance conditions’’ $\varepsilon_F - \varepsilon_{\mathbf{k}'} = \pm\Omega$ and $\varepsilon_F - \varepsilon_{\mathbf{k}} = \pm\Omega$.

Thus, the dominant scattering vectors in the presence of an electron-boson coupling are determined by the intersection points of the electron dispersion $\varepsilon_{\mathbf{k}}$ and the boson energy $\omega_{\mathbf{q}}$ (see Fig. 5). The corresponding Feynman diagram of this process is shown in the inset of Fig. 1(b). Note that in the actual numerical treatment the divergence is removed by taking into account contributions to the renormalization up to infinite order. Further note that the above considerations are also valid for a general momentum-dependent boson energy $\omega_{\mathbf{q}}$.

The same processes lead also to a renormalization of the electron dispersion. This can be seen again from its second-order perturbation theory result which has a similar form as expression (A2). As seen from Fig. 5(a) at the intersection points between the bare dispersion and the boson energy the renormalization is strongest and gives rise to a kinklike structure. This feature is also well known from several ARPES studies in cuprate and pnictide materials.

We have calculated all renormalized quantities in Eq. (A1) starting from a simplified model Hamiltonian \mathcal{H} with fixed parameters describing roughly the situation relevant to LiFeAs. The parameters of the free part \mathcal{H}_0 (related to some relevant energy unit) are a two-dimensional (2D) parabolic holelike dispersion $\varepsilon_{\mathbf{k}} = -k^2 + 0.2$ and a momentum-independent boson energy $\omega_{\mathbf{q}} = \Omega = 0.18$ lying slightly below the top of the fermion band. For the coupling parameters we have chosen the momentum-independent values $V = 0.1$ and $g = 0.1$. The numerical results are shown in Fig. 5(a). As already observed in the perturbation theory discussed above, a strong renormalization is found at the particular \mathbf{k} points where the original fermion band $\varepsilon_{\mathbf{k}}$ (red solid line) intersects with the values $\pm\Omega$ (dashed lines). This leads to kinklike structures in the renormalized fermion dispersion (black solid line) and, most importantly, to a strong enhancement of the elastic scattering potential (blue solid line). Thus, in the presence of an electron-boson interaction, the effective impurity scattering potential becomes strongly momentum dependent for a particular scattering momentum which is characterized by the resonant coupling to a virtual bosonic mode [compare the inset of Fig. 1(b)].

The calculated renormalized quantities $\tilde{\varepsilon}_{\mathbf{k}}$ and $\tilde{V}_{\mathbf{k},\mathbf{q}}$ can be used as input parameters for a subsequent standard t -matrix approach to calculate the Fourier-transformed local density of states,

$$\rho(\mathbf{q}, E) = \frac{1}{\pi} \sum_{\mathbf{k}} \Im G(\mathbf{k}, \mathbf{k} - \mathbf{q}, E), \quad (\text{A3})$$

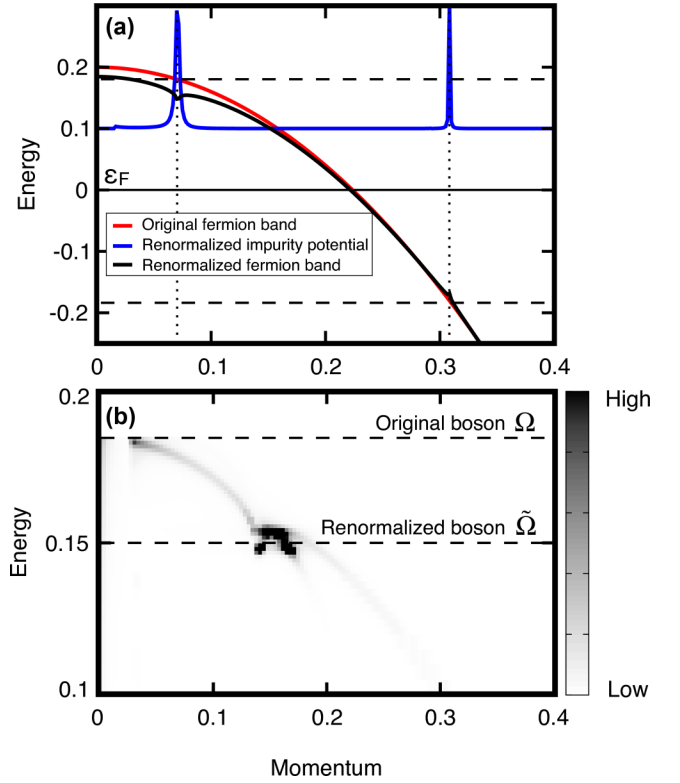


FIG. 5. Renormalization effects due to electron-boson coupling. (a) Renormalized fermion dispersion $\tilde{\varepsilon}_{\mathbf{k}}$ (black solid line) and impurity potential $\tilde{V}_{\mathbf{k},-\mathbf{k}}$ (blue solid line) combining opposite momentum vectors representing relevant elastic scattering processes calculated for a simplified holelike dispersion (red solid line). The momentum vector runs along the cut $\mathbf{k} = (k, 0)$. The particular \mathbf{k} points which fulfill the resonance condition $\varepsilon_F - \varepsilon_{\mathbf{k}} = \pm\Omega$ (indicated by the intersection points of the dashed lines with the original fermion band) give rise to strong renormalization of the impurity potential as well as the fermionic dispersion (kinklike structures). These pronounced momentum vectors are indicated by dotted lines. (b) Fourier-transformed local density of states as a function of scattering momentum calculated by a t -matrix method using the renormalized energy parameters from Eq. (1). The intensity is strongly enhanced around the particular scattering momentum combining the intersection points shown in (a). This exaggeration appears at the renormalized boson energy $\tilde{\Omega}$ which has decreased with respect to the original value Ω (dashed lines).

which is the quantity that is directly measured by STM/STS experiments. $G(\mathbf{k}, \mathbf{k}', E)$ is the retarded Green’s function in the presence of one single impurity and is related to the retarded Green’s function $G_0(\mathbf{k}, E)$ of the bulk material via the equation [41]

$$G(\mathbf{k}, \mathbf{k}', E) = G_0(\mathbf{k}, E) + G_0(\mathbf{k}, E)T_{\mathbf{k},\mathbf{k}'}(E)G_0(\mathbf{k}', E), \quad (\text{A4})$$

where the energy-dependent t -matrix $T_{\mathbf{k},\mathbf{k}'}(E)$ is determined by the following self-consistency equation,

$$T_{\mathbf{k},\mathbf{k}'}(E) = \tilde{V}_{\mathbf{k},\mathbf{k}'} + \sum_{\mathbf{k}''} \tilde{V}_{\mathbf{k},\mathbf{k}''}G_0(\mathbf{k}'', E)T_{\mathbf{k}'',\mathbf{k}'}(E). \quad (\text{A5})$$

The noninteracting Green’s function $G_0(\mathbf{k}, E) = (E - \tilde{\varepsilon}_{\mathbf{k}} - i\delta)^{-1}$ contains the renormalized fermion dispersion.

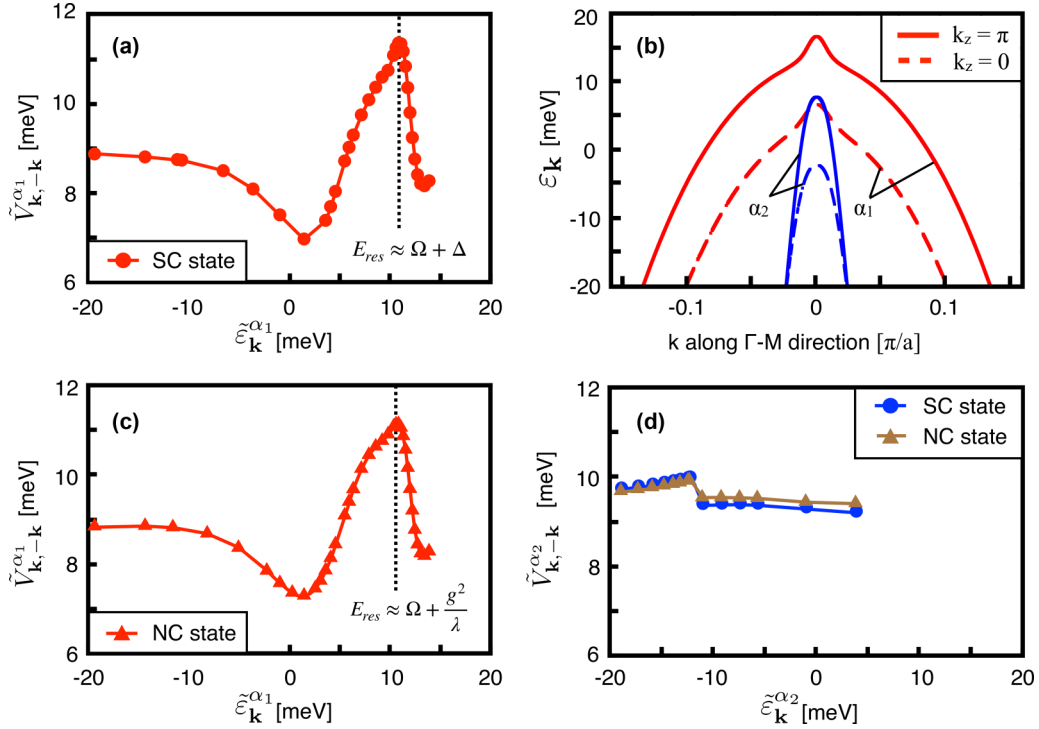


FIG. 6. Renormalized scattering potential in LiFeAs. (a) Renormalized impurity potential $\tilde{V}_{\mathbf{k},-\mathbf{k}}^{\alpha_1}$ combining opposite momentum vectors on the larger hole pocket α_1 plotted against the corresponding renormalized dispersion $\tilde{\epsilon}_{\mathbf{k}}^{\alpha_1}$ of the α_1 pocket. To allow for comparison with our measurements, the temperature is set to $T = 0.3$ K such that the system is in the superconducting (SC) state with a calculated gap of $\Delta = 5.5$ meV. The initial parameters are $V = 10$ meV for the impurity potential, $\omega = 8.5$ meV for the boson energy, and $g = 10.9$ meV for the electron-boson coupling strength. As confirmed by our QPI data the calculated scattering is resonantly enhanced at about 12 meV (dotted line) while it is significantly reduced in an energy range around the Fermi level. (b) Momentum cut (lattice constant a as defined in Fig. 2) of the two relevant holelike bands α_1 and α_2 in LiFeAs which are used as input parameters of the calculations. The dispersions are taken from the tight-binding model of Ref. [47] where the spin-orbit coupling in LiFeAs is included. (c) Renormalized impurity potential as in (a) but for the temperature $T = 25$ K where the system is in the normal conducting (NC) state. The resonance appears at roughly the same energy as in the superconducting state but is slightly broadened. Due to higher-order effects in combination with the characteristic spin-orbit splitting of the α bands, the resonance energy deviates approximately by the value g^2/λ (≈ 10 meV) from the boson energy as predicted from the perturbative result (A2). (d) Renormalized impurity potential as in (a) and (c) but referring to the smaller α_2 pocket.

Using as input parameters for our theory the two functions $G_0(\mathbf{k}, E)$ and $\tilde{V}_{\mathbf{k},\mathbf{k}'}$ we have solved the system of Eqs. (A4) and (A5) self-consistently. The obtained result for the full Green's function $G(\mathbf{k}, \mathbf{k}', E)$ is inserted in Eq. (A3) in order to evaluate the intensity $\rho(\mathbf{q}, E)$. The numerical result is shown in Fig. 5(b). In a large energy range the intensity is slightly enhanced for the scattering vectors combining momentum vectors with the same energy (conventional elastic scattering). There, the value of the scattering potential is nearly constant and therefore the intensity (gray shaded area) is mainly determined by the fermionic density of states while its momentum dependence is given by the dispersion $\tilde{\epsilon}_{\mathbf{k}}$ of the renormalized band. However, at scattering momentum nearly equal to the distance between the two inner peaks of $\tilde{V}_{\mathbf{k},-\mathbf{k}}$ in Fig. 5(b), the intensity is strongly enhanced (black area) due to the exaggeration of the renormalized scattering potential. Moreover, fine structures are visible which arise from the kink structure of $\tilde{\epsilon}_{\mathbf{k}}$ around the resonance points. Note that similar considerations have been also applied to study the pinning of dynamic spin-density-wave fluctuations where strong modulations in the local density of states could be traced back to the interaction with a correlated background medium [52,53].

Energetically, the resonance appears inside the kink feature of $\tilde{\epsilon}_{\mathbf{k}}$ which corresponds also to the minimum value of the renormalized boson energy $\tilde{\Omega} = \min(\tilde{\omega}_{\mathbf{q}})$. The numerical result of this energy level is shown in Fig. 5(b) by the lower dashed line. For the specific parameter values chosen in our calculation the momentum dependence of the renormalized boson energy $\tilde{\omega}_{\mathbf{q}}$ is rather weak and is therefore not shown here. Note, however, that such a dispersion may become important if the system is very close to a transition to ordered states [50].

2. Application to LiFeAs

To verify the measured positions of the resonance in LiFeAs in the superconducting as well as in the normal conducting state we have performed a careful analysis of the renormalized scattering potential based on realistic material parameters of LiFeAs. The results are shown in Fig. 6. For the input of the two relevant holelike bands α_1 and α_2 which are predominantly involved in the small-momentum impurity scattering, we have used the tight-binding model of Ref. [47] which includes also the spin-orbit interaction in

LiFeAs. However, to obtain a correct fitting to the small Fermi surfaces of the α bands as measured by ARPES [42], we have used the reduced value $\lambda = 10.5$ meV of the spin-orbit coupling parameter instead of the value 50 meV which has been used in Ref. [47] to optimally describe the electron pockets. The corresponding dispersions for $\lambda = 10.5$ meV are shown in Fig. 6(b). For the initial boson energy we have used the experimental value $\Omega = 8.5$ meV. The electron-boson coupling is fixed to $g = 10.9$ meV. This particular value is chosen as a result of a self-consistent superconducting solution of the Hamiltonian $\mathcal{H}_0 + \mathcal{H}_{eb}$ for the given realistic band structure and boson energy within the approach of Ref. [51]. For $g = 10.9$ meV such a self-consistent calculation leads at temperature $T = 0.3$ K to an s -wave gap of $\Delta = 5.5$ meV, which is equal to the gap as measured by our STM experiment.

Taking all the defined parameters as initial conditions we have evaluated separately the PRM renormalization equations for the backscattering impurity potentials $\tilde{V}_{\mathbf{k},-\mathbf{k}}^{\alpha_1}$ and $\tilde{V}_{\mathbf{k},-\mathbf{k}}^{\alpha_2}$ referring to states \mathbf{k} and $(-\mathbf{k})$ within the α_1 and α_2 band, respectively. Figures 6(a) and 6(c) show the renormalized impurity scattering potential for the α_1 band in the superconducting and normal conducting state, respectively. According to the mechanism described above, we find a resonantly enhanced scattering potential appearing in form of a maximum in $\tilde{V}_{\mathbf{k},-\mathbf{k}}^{\alpha_1}$ at a certain scattering momentum. In the superconducting state, this scattering momentum corresponds to an energy $\tilde{\varepsilon}_{\mathbf{k}}^{\alpha_1}$ that is as expected on an approximate level of $E_{\text{res}} \approx \Delta + \Omega \approx 12.8$ meV [dotted line in Fig. 6(a)], in agreement with the experiment. In the normal conducting state, however, the resonance is not seen exactly at Ω as perturbation theory predicts, but is shifted to a somewhat larger energy near the position in the superconducting state [dotted line in Fig. 6(c)]. This behavior is also very well consistent with our experimental results (compare Figs. 3, 11, and 12). The reason for such a shift is the influence of the higher-order contributions to the renormalized scattering potential, which is discussed in more detail below.

The resonance conditions derived above, $\varepsilon_F - \varepsilon_{\mathbf{k}} = \pm\Omega$ and $\varepsilon_F - \varepsilon_{\mathbf{k}} = \pm\Omega$, are the results of the specific form of the energy denominators in Eq. (A2) arising as a consequence of perturbation theory. The condition leads to a singularity in the renormalized impurity potential \tilde{V} which must be removed by the higher-order corrections. Schematically, according to Eq. (A2), the renormalization equation for the backscattering impurity potential $\tilde{V}_{\mathbf{k},-\mathbf{k}}$ has the following form in second-order perturbation theory,

$$\tilde{V}_{\mathbf{k},-\mathbf{k}}^{(2)} = V + \frac{V}{N} \sum_{\mathbf{q}} \frac{g^2}{\Delta E_{\mathbf{k},\mathbf{q}} \Delta E_{-\mathbf{k},\mathbf{q}}} + \dots, \quad (\text{A6})$$

where $\Delta E_{\mathbf{k},\mathbf{q}}$ is an energy denominator which includes the energy difference between electron states and the boson energy. The dots indicate more terms of the same structure. According to the above discussion, the conditions $\Delta E_{\pm\mathbf{k},\mathbf{q}} = 0$ are responsible for the observed resonance in the impurity scattering for a particular combination of the momentum vectors \mathbf{k} and \mathbf{q} .

We now discuss the influence of the higher-order contributions to the perturbative result (A6). According to the method of continued fractions (see, for example, Ref. [54]) which

can be considered for the solution of integral equations, the higher-order correction to an arbitrary energy denominator ΔE is $\Delta E + g^2/\Delta E'$, where the correction $g^2/\Delta E'$ must be continued to all denominators up to infinite order, i.e., $\Delta E' = \Delta E + g^2/\Delta E''$, $\Delta E'' = \Delta E + g^2/\dots$. Thus, the corresponding higher-order correction of Eq. (A6) reads

$$\tilde{V}_{\mathbf{k},-\mathbf{k}} = V + \frac{V}{N} \sum_{\mathbf{q}} \frac{g^2}{(\Delta E_{\mathbf{k},\mathbf{q}} + \frac{1}{N} \sum_{\mathbf{q}'} \frac{g^2}{\Delta E_{\mathbf{k},\mathbf{q}'}})(\dots)} + \dots, \quad (\text{A7})$$

where the factor (\dots) denotes an equivalent factor with \mathbf{k} replaced by $-\mathbf{k}$. As can be seen easily from the change of the energy denominator in Eq. (A7), such a correction leads immediately to a shift of the resonance condition from $\Delta E_{\pm\mathbf{k},\mathbf{q}} = 0$ (as in perturbation theory) to

$$\Delta E_{\pm\mathbf{k},\mathbf{q}} + \frac{1}{N} \sum_{\mathbf{q}'} \frac{g^2}{\Delta E_{\pm\mathbf{k},\mathbf{q}'}} = 0, \quad (\text{A8})$$

where the energy denominator has the particular form $\Delta E_{\pm\mathbf{k},\mathbf{q}} = \varepsilon_{\pm\mathbf{k}} - \varepsilon_{\pm\mathbf{k}+\mathbf{q}} + \Omega$ in a one-band system. Equation (A8) enables to estimate the higher-order correction to the perturbation theory value of the resonance energy. We start with the simplest case of a usual metal. In this case $\Delta E_{\pm\mathbf{k},\mathbf{q}'}$ is of the order of (eV) for most of the momentum vectors \mathbf{q}' in the momentum summation since for a given $\pm\mathbf{k}$ the energy difference $\varepsilon_{\pm\mathbf{k}} - \varepsilon_{\pm\mathbf{k}+\mathbf{q}'}$ combines high-energy states for a macroscopic amount (order of N) of \mathbf{q}' points. Thus, according to Eq. (A8), for a usual one-band metal the correction is of the order g^2 /(eV), which is usually a very small value. For such a material the perturbation theory is valid. However, the situation changes in the superconducting state where, due to the presence of the superconducting gap Δ , a macroscopic number of states gives rise to energy transitions $\Delta E_{\pm\mathbf{k},\mathbf{q}'}$ of the order of Δ . In the case of superconducting LiFeAs, the correction to the resonance condition in Eq. (A8) is also of the order of Δ since $g \approx 10$ meV. This explains the shift of the resonance in the superconducting state from Ω to roughly $\Omega + g^2/\Delta \approx \Omega + \Delta$.

In the normal conducting state of LiFeAs we would expect a shift according to the same arguments. This is due to the specific band structure in LiFeAs. As can be seen in Fig. 6(b), there is a large density of states around the Γ point where the α bands have maximum values. However, in this region the spin-orbit splitting is significant and also of the order of 10 meV (as the superconducting gap). Thus, the correction to the perturbative resonance condition in the normal conducting state is of the same order as in the superconducting state, which is clearly seen in a comparison between Figs. 6(a) and 6(c).

Furthermore, one can recognize a characteristic depletion of $\tilde{V}_{\mathbf{k},-\mathbf{k}}^{\alpha_1}$ in a region around the Fermi level. This feature is again a consequence of the specific band structure and can be understood as follows. Due to the relatively strong k_z dispersion of both bands [compare solid and dashed lines in Fig. 6(b)], the top of the α_1 band ranges from about 8 to 16 meV. Thus, for scattering energies below about 8 meV, the sign of the dominant energy denominators, which involve states around the top of the band, can change.

Moreover, at negative energies no further resonance is found for the α_1 band, which is also in agreement with the experiment. Instead, such a resonance is found in a much weaker form on the α_2 band as shown in Fig. 6(d). This is the reason why in our QPI measurements the feature at negative bias voltage appears at a similar momentum as the main resonance feature on the positive side. This observation suggests that the involved boson, which leads to the exaggerated impurity scattering and at the same time mediates the superconducting pairing, must have a very small momentum \mathbf{q} .

In our QPI measurements the intensity of the resonance at positive energy is exaggerated in comparison with the usual QPI at a larger momentum or negative energy. As discussed in Fig. 6, such an amplification is clearly seen also in our theoretical model by a significant variation of $\tilde{V}_{\mathbf{k},-\mathbf{k}}^{\alpha_1}$ by a factor of around 2. This amount of variation is sufficient to explain the observed resonance behavior in the QPI measurements for the following reasons. First, note that the QPI intensity is not only determined by the renormalized scattering potential but also by the density of states which is enhanced near the band maximum of the α bands. Moreover, additional contributions to the QPI are given by multiple scattering processes, which become particularly important in the presence of a strong scattering potential. Thus, a consistent calculation of the QPI intensity requires in this case the self-consistent inclusion of higher-order scattering processes by a standard t -matrix approach. Such treatments are known to boost the QPI intensity particularly at energies around a resonance. These reasons altogether lead to the conclusion that our calculated variation of the scattering potential can fully explain our measured resonance behavior in the QPI of LiFeAs.

In summary, our theoretical considerations allow us to explain the characteristic intensity distribution of the observed

resonance features as follows: The resonantly enhanced QPI signal in the unoccupied energy range stems from the impurity scattering between states of the α_1 band. Thereby, also states of the α_2 band which are placed extremely close to the Fermi level are involved through the virtually excited boson. These processes lead to the particularly strong renormalization of the scattering potential at positive energy. This is, however, not the case for the resonance in the occupied region since here, due to the specific band structure of LiFeAs, the virtual states cannot be placed at such a vicinity to the Fermi level

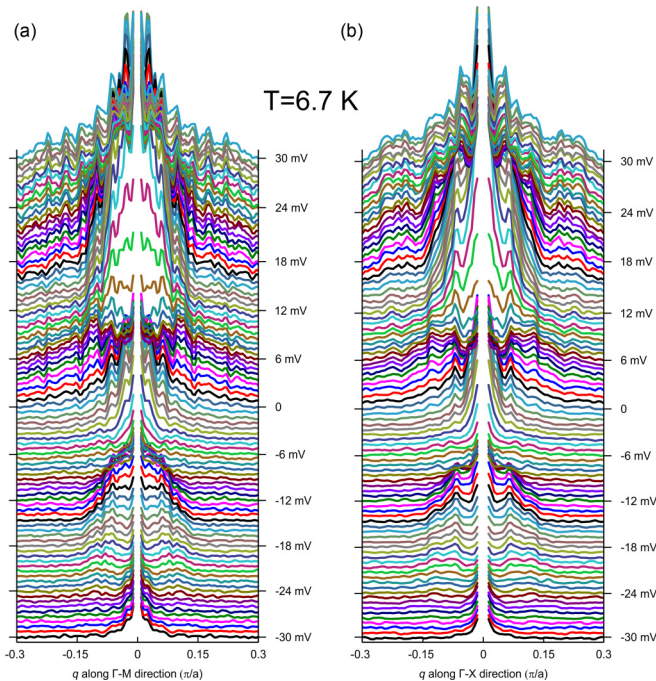


FIG. 7. Waterfall representation of the FT-STS data taken at 6.7 K. (a) Along Γ - M , and (b) along Γ - X .

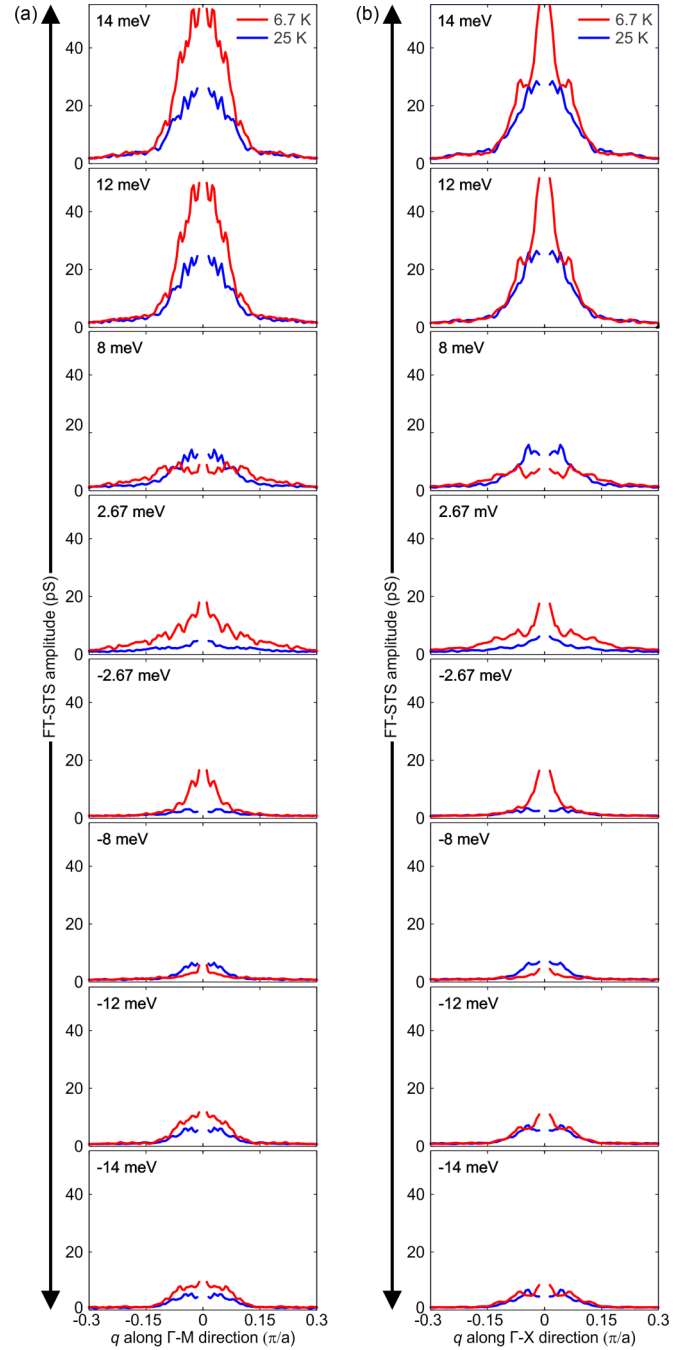


FIG. 8. Amplitude of the FT-STS data for selected energies at 6.7 and at 25 K. Columns (a) and (b) show the data along the Γ - M and Γ - X directions, respectively.

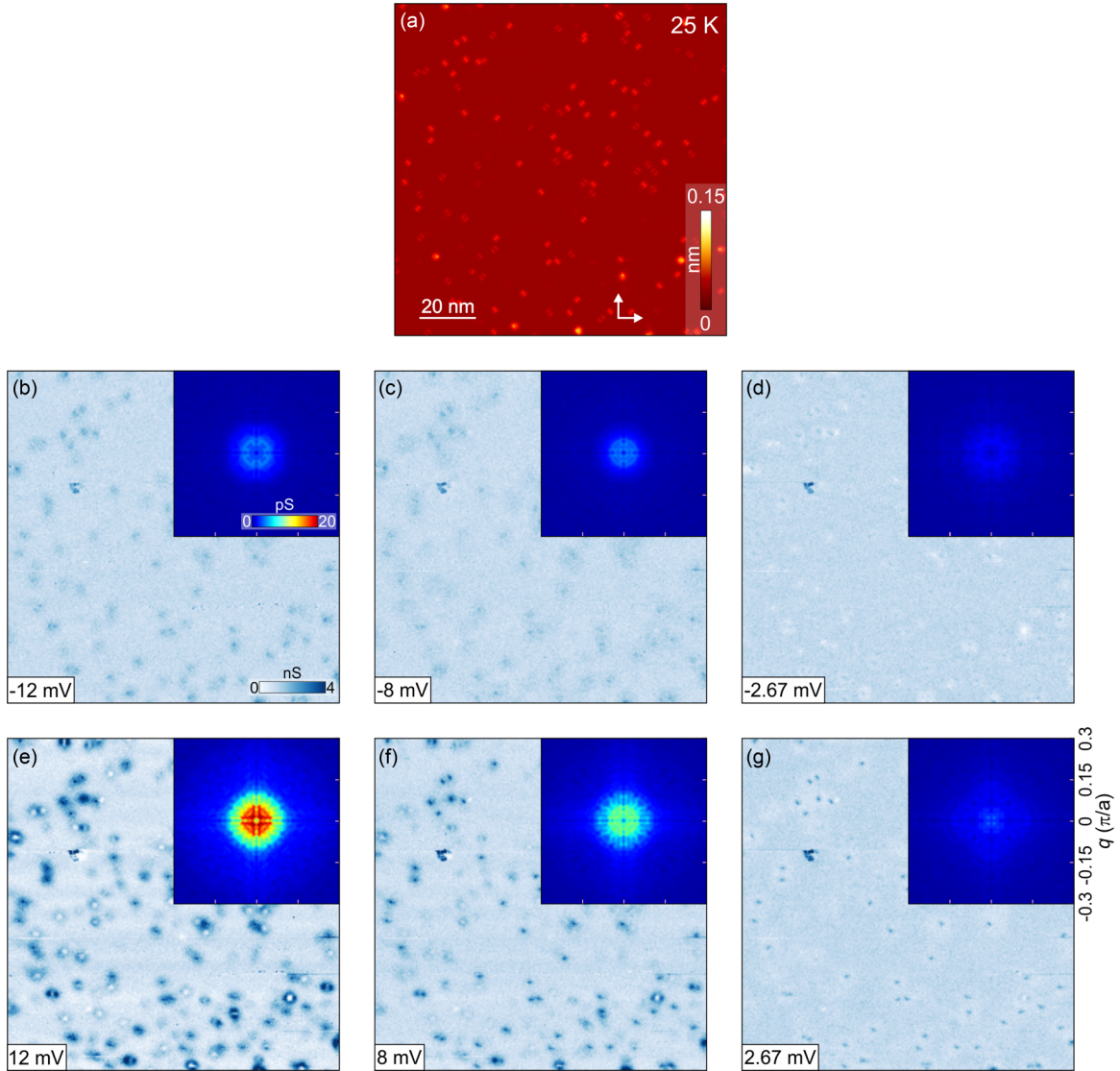


FIG. 9. Experimental data in the normal conducting state at $T = 25$ K. (a) Representative surface topography ($U_{\text{bias}} = -50$ mV, $I = 100$ pA) of the sample surface. The directions of the shortest Fe-Fe distance are indicated by arrows. (b)–(g) Real-space conductance map at selected energies $eU_{\text{bias}} = \pm 12, \pm 8, \text{ and } \pm 2.67$ meV. The conductance map is taken in the same area shown in (a). The Fourier transformation of the real-space conductance map data is shown in the corresponding insets.

and consequently the resonance appears here with much less intensity.

APPENDIX B: EXPERIMENTAL DETAILS

1. Sample preparation

Single crystals of stoichiometric LiFeAs have been grown using the self-flux method as described in Ref. [55]. In order to ensure stoichiometry and homogeneity of the sample, we confirmed the ^{75}As nuclear quadrupole resonance (NQR) frequency and linewidth of the sample as 21.561 ± 0.001 MHz and 31 ± 1 kHz, respectively [8]. Since LiFeAs is highly air sensitive, these steps, and the mounting of the sample into our scanning tunneling microscope, have been performed in Ar atmosphere.

2. Scanning tunneling microscopy/spectroscopy measurements

The STM measurements are carried out in two home-built low-temperature scanning tunneling microscopes using a tungsten tip. One of the microscopes is optimized for QPI data acquisition at variable temperatures [56]. All QPI and point spectroscopy data at temperatures between 6.7 and 25 K have been obtained with this instrument on one single crystal of LiFeAs. The other [57] has been used for measuring the 300-mK point spectroscopy data on another LiFeAs crystal.

Atomically flat LiFeAs surfaces were obtained by cleaving the crystal inside the scanning tunneling microscope in cryogenic vacuum or ultrahigh vacuum. For all tunneling conductance spectra, we used a lock-in amplifier with a modulation of 0.4 mV_{rms} at 1.1111 kHz. The 300-mK measurements were performed with various modulation voltages between 0.4 mV_{rms} and 40 μV _{rms}. However, no significant change in

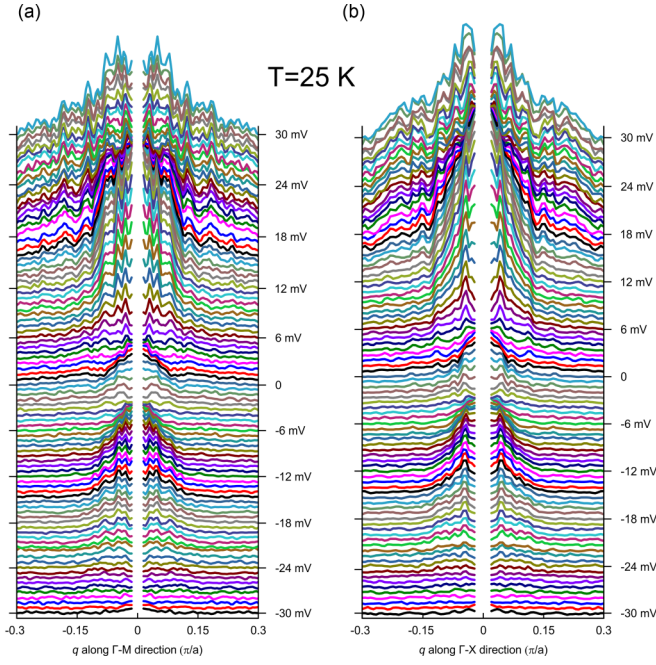


FIG. 10. Waterfall representation of the FT-STs data taken at 25 K. (a) Along Γ - M , and (b) along Γ - X .

the width of the coherence peaks could be observed with lower modulation amplitudes. Conductance maps are taken with a grid size of 256×256 pixels. All the spectroscopic maps are taken with stabilization condition of $U_{\text{bias}} = -50$ mV and $I_T = 600$ pA. Each spectroscopic map is measured over the energy range between ± 30 mV with consecutive energy point spacings of 0.67 mV. The total time for acquiring one spectroscopic map was about 3.5 days. Prior to each spectroscopic map measurement, the microscope was stabilized at the respective temperature for a sufficient time until a stable drift of the tip with respect to the sample was reached. At base temperature (6.7 K) the drift was immeasurably small, whereas at 25 K the drift was lower than $2a$ per day.

3. Data processing

The FT-STs data are calculated as the amplitude of the fast Fourier transform of the AC part of each energy slice of the real-space spectroscopy map. Symmetrized FT-STs data sets and images are subsequently achieved by symmetrizing the raw FT-STs data along both the two lattice high-symmetry directions (Γ - X and Γ - M) [as shown in Fig. 2(c)]. In order to enhance the contrast of the QPI pattern, we have applied a (5×5) linear convolution to the symmetrized QPI data, from which the line cuts in Figs. 3(a)–3(d) have been derived.

APPENDIX C: ADDITIONAL EXPERIMENTAL DATA

1. Superconducting state at 6.7 K

The whole data set at base temperature (6.7 K), of which Fig. 2 shows selected energy slices, is visualized in Movie S1 in the Supplemental Material [39]. In order to further visualize the energy and momentum dependence of the amplitude of the FT-STs data, we show, complementary to Figs. 3(a) and

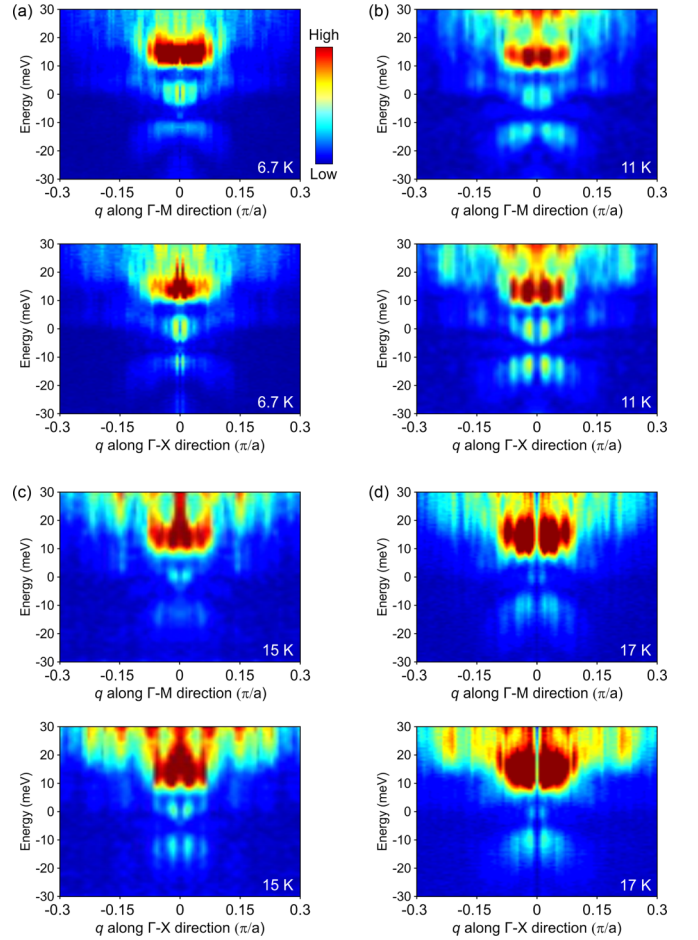


FIG. 11. Energy-momentum dependence of FT-STs data along high-symmetry directions. (a)–(d) correspond to 6.7, 11, 15, and 17 K, respectively.

3(b), in Fig. 7 a waterfall representation of these data along the Γ - M direction [Fig. 7(a)] and along the Γ - X direction [Fig. 7(b)].

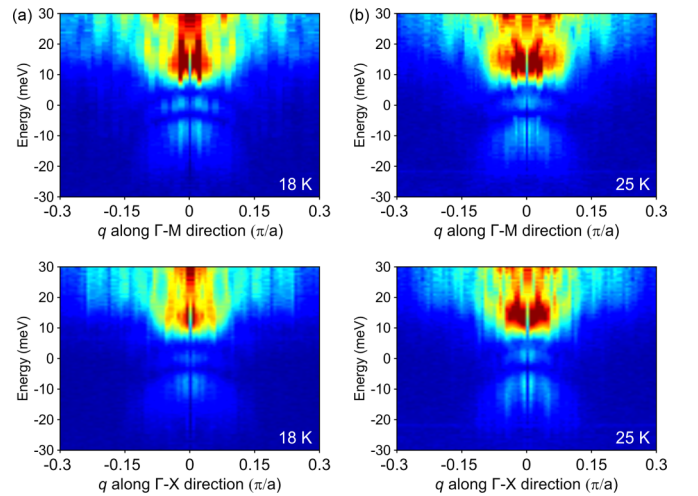


FIG. 12. Energy-momentum dependence of FT-STs data along high-symmetry directions. (a) and (b) correspond to 18 and 25 K, respectively.

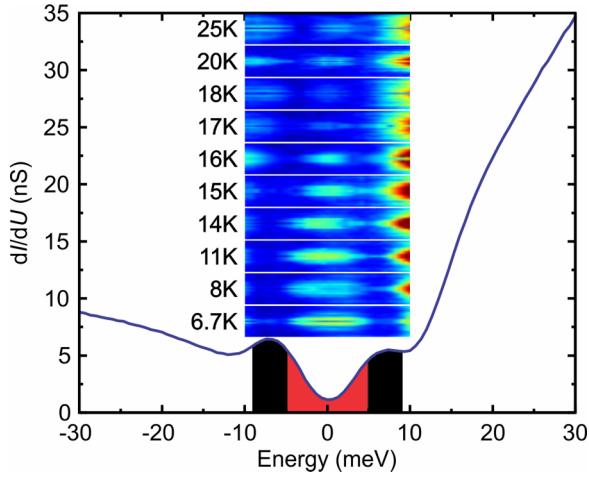


FIG. 13. Temperature evolution of feature (i). Representative dI/dU spectrum on the bare surface at 6.7 K highlighting the size of Δ_1 (red bar) in comparison to feature (i). Inset: Zoom-in into the area spanned by momentum $q = \pm 0.086\pi/a$ and energy $eU_{\text{bias}} = \pm 10$ meV for each temperature of the line cuts shown in Figs. 11 and 12 and for further temperatures along the Γ - M direction.

Figure 8 depicts the amplitude of the FT-STs data in the superconducting state at 6.7 K for selected energies in line cuts along Γ - M and Γ - X in order to highlight the strong enhancement of the amplitude at energies larger than about 10 meV, and to demonstrate the decay of the amplitude as a function of q .

2. Normal conducting state at 25 K

Figure 9 shows the topography and selected energy slices in real space and the corresponding Fourier-transformed data of the conductance map measured in the normal state at 25 K. Based on these results, the low-temperature (6.7 K) data in Fig. 8 are complemented by analogous data for the normal conducting state at 25 K. Evidently, the FT-STs amplitude remains large at energies larger than 10 meV, whereas the amplitude enhancement due the impurity bound state has vanished (± 2.67 meV). In order to further visualize the energy and momentum dependence of the amplitude of the FT-STs data, we show, complementary to Figs. 3(c) and 3(d), in

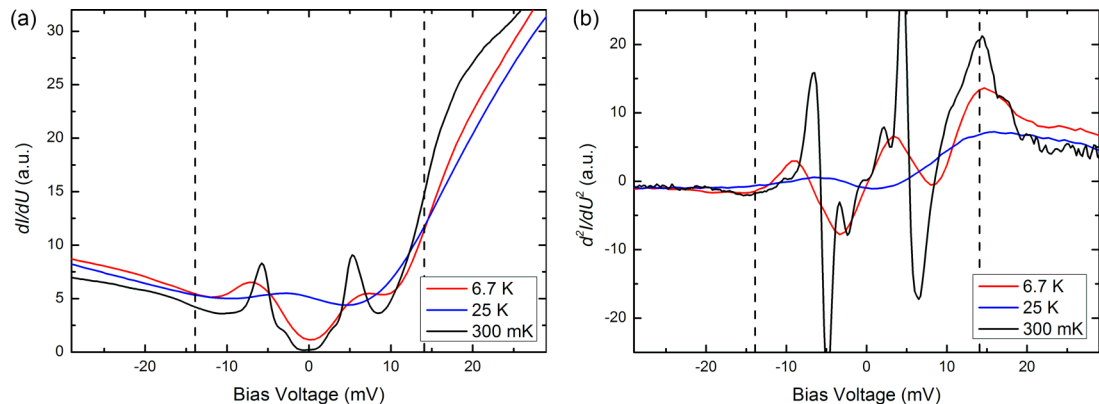


FIG. 14. Low-temperature point spectroscopy. Comparison of 300-mK point spectroscopy data with those shown in Figs. 4(d) and 4(e). (a) dI/dU data at 300 mK, 6.7 K, and 25 K. (b) Second derivative d^2I/dU^2 for the same temperatures.

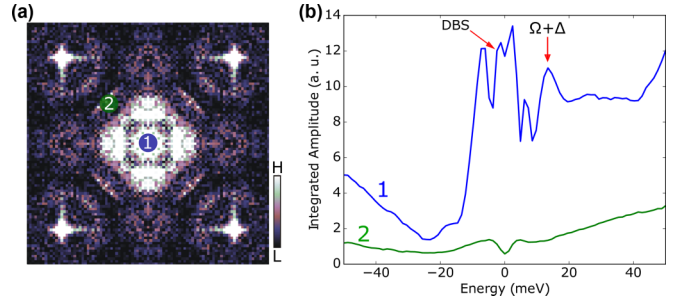


FIG. 15. Comparison of feature (ii) with QPI signals at larger q . (a) Representative FT-STs data (the same as published in Ref. [23]) at -14.1 meV. The small- q area which is at the focus of this work is indicated by the blue filled area “1”. The green filled area “2” is located around those q where intraband scattering of the γ band is located (labeled q_4 in Ref. [23]). Apparently, this intraband scattering generates a particularly sharp and intense QPI signal, which is caused by a significant nesting of the band (cf. Fig. 1). We integrate the amplitudes at areas 1 and 2 and plot the integrated amplitude in (b) as a function of energy. Clearly, the integrated amplitude around 2 remains significantly lower than that of area 1. In particular, a pronounced peak at $\Omega + \Delta$ corresponding to feature (ii) of the current study is visible, in addition to clear signatures due to defect bound states (DBS).

Fig. 10 a waterfall representation of the FT-STs data along the Γ - M direction [Fig. 10(a)] and along the Γ - X direction [Fig. 10(b)].

Figure 8 depicts the amplitude of the FT-STs data for selected energies in order to highlight the strong enhancement of the amplitude at energies larger than about 10 meV, and to demonstrate the decay of the amplitude as a function of q . An overall smaller amplitude as compared to that at 6.7 K is evident.

3. Temperature-dependent FT-STs data

dI/dU maps of $110 \text{ nm} \times 110 \text{ nm}$ areas have been measured in the temperature range between 6.7 and 25 K at ten specific temperatures. The resulting energy-momentum dependence of the FT-STs data at selected energies is shown in Figs. 11 and 12 as line cuts along high-symmetry directions

analogous to Figs. 3(a) and 3(b). These data show quite clearly that feature (ii) remains present at all temperatures and even in the normal conducting state, whereas feature (i) vanishes at the critical temperature $T_c \approx 18$ K. The latter is further visualized in Fig. 13.

4. Low-temperature point spectroscopy

Figure 14 shows a comparison of the 300 mK point spectroscopy data of Fig. 2(a) with those shown in Figs. 4(d) and 4(e). The dI/dU data at 300 mK apparently are a systematic low-temperature evolution of the data at 6.7 K, since the coherence peaks of the large gap Δ_1 and of the small gap Δ_2 become clearly discernible [Fig. 14(a)]. The second derivative d^2I/dU^2 shown in Fig. 14(b) underpins the sharpening of the spectral features at $|eU| \lesssim \Delta_1$. In contrast, the width of the

steplike increase in dI/dU at about 14 mV reduces only by a small amount upon cooling from 6.7 K to 300 mK, as is revealed by the corresponding peaks in d^2I/dU^2 .

APPENDIX D: COMPARISON OF FEATURE (ii) WITH STANDARD QPI AT LARGER q

Figure 15 shows a comparison of the integrated amplitude of feature (ii) with that of standard QPI. For this comparison, we analyzed our previous LiFeAs data [23] which include such large- q QPI information. The inspection of these data clearly confirm the presence of feature (ii) and furthermore reveal that feature (ii) is significantly more intense than standard QPI.

-
- [1] W. L. McMillan and J. M. Rowell, *Phys. Rev. Lett.* **14**, 108 (1965).
- [2] D. J. Scalapino, J. R. Schrieffer, and J. W. Wilkins, *Phys. Rev.* **148**, 263 (1966).
- [3] E. W. Hudson, S. H. Pan, A. K. Gupta, K.-W. Ng, and J. C. Davis, *Science* **285**, 88 (1999).
- [4] N. Jenkins, Y. Fasano, C. Berthod, I. Maggio-Aprile, A. Piriou, E. Giannini, B. W. Hoogenboom, C. Hess, T. Cren, and O. Fischer, *Phys. Rev. Lett.* **103**, 227001 (2009).
- [5] Z. Wang, H. Yang, D. Fang, B. Shen, Q.-H. Wang, L. Shan, C. Zhang, P. Dai, and H.-H. Wen, *Nat. Phys.* **9**, 42 (2013).
- [6] C.-L. Song, Y.-L. Wang, Y.-P. Jiang, Z. Li, L. Wang, K. He, X. Chen, J. E. Hoffman, X.-C. Ma, and Q.-K. Xue, *Phys. Rev. Lett.* **112**, 057002 (2014).
- [7] S. Chi, S. Grothe, R. Liang, P. Dosanjh, W. N. Hardy, S. A. Burke, D. A. Bonn, and Y. Pennec, *Phys. Rev. Lett.* **109**, 087002 (2012).
- [8] P. K. Nag, R. Schlegel, D. Baumann, H.-J. Grafe, R. Beck, S. Wurmehl, B. Büchner, and C. Hess, *Sci. Rep.* **6**, 27926 (2016).
- [9] P. Hlobil, J. Jandke, W. Wulfhekkel, and J. Schmalian, *Phys. Rev. Lett.* **118**, 167001 (2017).
- [10] D. C. Johnston, *Adv. Phys.* **59**, 803 (2010).
- [11] R. M. Fernandes, A. V. Chubukov, and J. Schmalian, *Nat. Phys.* **10**, 97 (2014).
- [12] I. I. Mazin, D. J. Singh, M. D. Johannes, and M. H. Du, *Phys. Rev. Lett.* **101**, 057003 (2008).
- [13] H. Kontani and S. Onari, *Phys. Rev. Lett.* **104**, 157001 (2010).
- [14] D. S. Inosov, J. T. Park, P. Bourges, D. L. Sun, Y. Sidis, A. Schneidewind, K. Hradil, D. Haug, C. T. Lin, B. Keimer *et al.*, *Nat. Phys.* **6**, 178 (2010).
- [15] W. Li, Y. Zhang, P. Deng, Z. Xu, S.-K. Mo, M. Yi, H. Ding, M. Hashimoto, R. G. Moore, D.-H. Lu *et al.*, *Nat. Phys.* **13**, 957 (2017).
- [16] C. M. Yim, C. Trainer, R. Aluru, S. Chi, W. N. Hardy, R. Liang, D. Bonn, and P. Wahl, *Nat. Commun.* **9**, 2602 (2018).
- [17] S. Lederer, Y. Schattner, E. Berg, and S. A. Kivelson, *Phys. Rev. Lett.* **114**, 097001 (2015).
- [18] Y. Schattner, S. Lederer, S. A. Kivelson, and E. Berg, *Phys. Rev. X* **6**, 031028 (2016).
- [19] Y. Wang, A. Kreisel, V. B. Zabolotnyy, S. V. Borisenko, B. Büchner, T. A. Maier, P. J. Hirschfeld, and D. J. Scalapino, *Phys. Rev. B* **88**, 174516 (2013).
- [20] J. E. Hoffman, K. McElroy, D.-H. Lee, K. M. Lang, H. Eisaki, S. Uchida, and J. C. Davis, *Science* **297**, 1148 (2002).
- [21] P. Aynajian, E. H. da Silva Neto, A. Gyenis, R. E. Baumbach, J. D. Thompson, Z. Fisk, E. D. Bauer, and A. Yazdani, *Nature (London)* **486**, 201 (2012).
- [22] M. P. Allan, A. W. Rost, A. P. Mackenzie, Y. Xie, J. C. Davis, K. Kihou, C. H. Lee, A. Iyo, H. Eisaki, and T.-M. Chuang, *Science* **336**, 563 (2012).
- [23] T. Hänke, S. Sykora, R. Schlegel, D. Baumann, L. Harnagea, S. Wurmehl, M. Daghofer, B. Büchner, J. van den Brink, and C. Hess, *Phys. Rev. Lett.* **108**, 127001 (2012).
- [24] C. Hess, S. Sykora, T. Hänke, R. Schlegel, D. Baumann, V. B. Zabolotnyy, L. Harnagea, S. Wurmehl, J. van den Brink, and B. Büchner, *Phys. Rev. Lett.* **110**, 017006 (2013).
- [25] S. Grothe, S. Johnston, S. Chi, P. Dosanjh, S. A. Burke, and Y. Pennec, *Phys. Rev. Lett.* **111**, 246804 (2013).
- [26] M. P. Allan, K. Lee, A. W. Rost, M. H. Fischer, F. Massee, K. Kihou, C.-H. Lee, A. Iyo, H. Eisaki, T.-M. Chuang *et al.*, *Nat. Phys.* **11**, 177 (2015).
- [27] Z. Wang, D. Walkup, P. Derry, T. Scaffidi, M. Rak, S. Vig, A. Kogar, I. Zeljkovic, A. Husain, L. H. Santos *et al.*, *Nat. Phys.* **13**, 799 (2017).
- [28] S. V. Borisenko, V. B. Zabolotnyy, D. V. Evtushinsky, T. K. Kim, I. V. Morozov, A. N. Yaresko, A. A. Kordyuk, G. Behr, A. Vasiliev, R. Follath *et al.*, *Phys. Rev. Lett.* **105**, 067002 (2010).
- [29] B. Zeng, D. Watanabe, Q. R. Zhang, G. Li, T. Besara, T. Siegrist, L. Y. Xing, X. C. Wang, C. Q. Jin, P. Goswami *et al.*, *Phys. Rev. B* **88**, 144518 (2013).
- [30] S. Aswartham, G. Behr, L. Harnagea, D. Bombor, A. Bachmann, I. V. Morozov, V. B. Zabolotnyy, A. A. Kordyuk, T. K. Kim, D. V. Evtushinsky *et al.*, *Phys. Rev. B* **84**, 054534 (2011).
- [31] M. J. Pitcher, T. Lancaster, J. D. Wright, I. Franke, A. J. Steele, P. J. Baker, F. L. Pratt, W. T. Thomas, D. R. Parker, S. J. Blundell *et al.*, *J. Am. Chem. Soc.* **132**, 10467 (2010).
- [32] N. Qureshi, P. Steffens, Y. Drees, A. C. Komarek, D. Lamago, Y. Sidis, L. Harnagea, H.-J. Grafe, S. Wurmehl, B. Büchner *et al.*, *Phys. Rev. Lett.* **108**, 117001 (2012).

- [33] J. Knolle, V. B. Zabolotnyy, I. Eremin, S. V. Borisenko, N. Qureshi, M. Braden, D. V. Evtushinsky, T. K. Kim, A. A. Kordyuk, S. Sykora *et al.*, *Phys. Rev. B* **86**, 174519 (2012).
- [34] F. Ahn, I. Eremin, J. Knolle, V. B. Zabolotnyy, S. V. Borisenko, B. Büchner, and A. V. Chubukov, *Phys. Rev. B* **89**, 144513 (2014).
- [35] S. V. Borisenko, V. B. Zabolotnyy, A. A. Kordyuk, D. V. Evtushinsky, T. K. Kim, I. V. Morozov, R. Follath, and B. Büchner, *Symmetry* **4**, 251 (2012).
- [36] S. Chi, S. Johnston, G. Levy, S. Grothe, R. Szedlak, B. Ludbrook, R. Liang, P. Dosanjh, S. A. Burke, A. Damascelli *et al.*, *Phys. Rev. B* **89**, 104522 (2014).
- [37] S. Grothe, S. Chi, P. Dosanjh, R. Liang, W. N. Hardy, S. A. Burke, D. A. Bonn, and Y. Pennec, *Phys. Rev. B* **86**, 174503 (2012).
- [38] R. Schlegel, P. K. Nag, D. Baumann, R. Beck, S. Wurmehl, B. Büchner, and C. Hess, *Phys. Status Solidi B* **254**, 1600159 (2017).
- [39] See Supplemental Material at <http://link.aps.org/supplemental/10.1103/PhysRevB.100.024506> for an overview of the full data set (movie).
- [40] S. Chi, R. Aluru, S. Grothe, A. Kreisel, U. R. Singh, B. M. Andersen, W. N. Hardy, R. Liang, D. A. Bonn, S. A. Burke *et al.*, *Nat. Commun.* **8**, 15996 (2017).
- [41] A. V. Balatsky, I. Vekhter, and J.-X. Zhu, *Rev. Mod. Phys.* **78**, 373 (2006).
- [42] S. V. Borisenko, D. V. Evtushinsky, Z.-H. Liu, I. Morozov, R. Kappenberger, S. Wurmehl, B. Büchner, A. N. Yaresko, T. K. Kim, M. Hoesch *et al.*, *Nat. Phys.* **12**, 311 (2016).
- [43] We estimate the error for Ω from the width of the peak at $\Delta_1 + \Omega$ in Figs. 3(f) and 4(e).
- [44] J. Hwang, J. P. Carbotte, B. H. Min, Y. S. Kwon, and T. Timusk, *J. Phys.: Condens. Matter* **27**, 055701 (2015).
- [45] P. M. R. Brydon, M. Daghofer, C. Timm, and J. van den Brink, *Phys. Rev. B* **83**, 060501(R) (2011).
- [46] Z. P. Yin, K. Haule, and G. Kotliar, *Nat. Phys.* **10**, 845 (2014).
- [47] T. Saito, Y. Yamakawa, S. Onari, and H. Kontani, *Phys. Rev. B* **92**, 134522 (2015).
- [48] Y. S. Kushnirenko, D. V. Evtushinsky, T. K. Kim, I. V. Morozov, L. Harnagea, S. Wurmehl, S. Aswartham, A. V. Chubukov, S. V. Borisenko, [arXiv:1810.04446](https://arxiv.org/abs/1810.04446).
- [49] K. W. Becker, A. Hübsch, and T. Sommer, *Phys. Rev. B* **66**, 235115 (2002).
- [50] S. Sykora, A. Hübsch, K. W. Becker, G. Wellein, and H. Fehske, *Phys. Rev. B* **71**, 045112 (2005).
- [51] D.-N. Cho, J. van den Brink, H. Fehske, K. W. Becker, and S. Sykora, *Sci. Rep.* **6**, 22548 (2016).
- [52] A. Polkovnikov, M. Vojta, and S. Sachdev, *Phys. Rev. B* **65**, 220509(R) (2002).
- [53] E. Rossi and D. K. Morr, *Phys. Rev. B* **81**, 054443 (2010).
- [54] J. Horáček and T. Sasakawa, *Phys. Rev. A* **28**, 2151 (1983).
- [55] I. Morozov, A. Boltalin, O. Volkova, A. Vasiliev, O. Kataeva, U. Stockert, M. Abdel-Hafiez, D. Bombor, A. Bachmann, L. Harnagea *et al.*, *Cryst. Growth Des.* **10**, 4428 (2010).
- [56] R. Schlegel, T. Hänke, D. Baumann, M. Kaiser, P. K. Nag, R. Voigtländer, D. Lindackers, B. Büchner, and C. Hess, *Rev. Sci. Instrum.* **85**, 013706 (2014).
- [57] C. Salazar, D. Baumann, T. Hänke, M. Scheffler, T. Kühne, M. Kaiser, R. Voigtländer, D. Lindackers, B. Büchner, and C. Hess, *Rev. Sci. Instrum.* **89**, 065104 (2018).